Cell type-specific inhibitory modulation of sound processing in the auditory thalamus.

Rolón-Martínez, S[1#]., Mendoza, A.J.[2#], Angeloni, C.F.[1], Vogler, N.W. [1], Drotos, A.C.[1], Aizenberg, M.[1], Chen, R.[1], Vu, K. [2], Haas, J.S.[2#], Geffen M.N.[1#] *

[1]*Department of Otorhinolaryngology, University of Pennsylvania, Philadelphia, PA, United States*

[2]*Department of Biological Sciences, Lehigh University, Bethlehem, PA, United States*

 # These authors contributed equally.

*Corresponding author:
Maria Neimark Geffen, Ph.D. (she/her)
Department of Otorhinolaryngology
Perelman School of Medicine
University of Pennsylvania
5 Ravdin
3400 Spruce St.
Philadelphia PA 19104
Tel.: 215.898.0782

ABSTRACT

Inhibition plays an important role in controlling the flow and processing of auditory information throughout the central auditory pathway, yet how inhibitory circuits shape auditory processing in the medial geniculate body (MGB), the key region in the auditory thalamus, is poorly understood. The MGB gates the flow of auditory information to the auditory cortex, and it is inhibited largely by the thalamic reticular nucleus (TRN). The TRN contains two major classes of inhibitory neurons: parvalbumin (PV^{TRN})-positive and somatostatin (SST^{TRN})-positive neurons. PV and SST neurons have been shown to play differential roles in controlling sound responses in auditory cortex. In the somatosensory and visual subregions of the TRN, PV^{TRN} and SST^{TRN} neurons exhibit anatomical and functional differences. However, it remains unknown whether and how PV^{TRN} and SST^{TRN} neurons differ in their anatomical projections from the TRN to the *auditory* thalamus, and whether and how they differentially modulate activity in the MGB. We find that PV^{TRN} and SST^{TRN} neurons exhibit differential projection patterns within the auditory thalamus: PV^{TRN} neurons predominantly project to ventral MGB, whereas SST^{TRN} neurons project to the dorso-medial regions of MGB. Optogenetic inactivation of PV^{TRN} neurons bidirectionally modulated sound-evoked activity in MGB, increasing firing in 29% of MGB neurons, while suppressing firing in 41%. In contrast, inactivating SST^{TRN} neurons largely suppressed tone-evoked activity in MGB neurons. Cell type-specific computational models identified candidate circuit mechanisms for generating the differential effects of TRN inactivation on MGB sound responses. These distinct inhibitory pathways within the auditory thalamus reveal cell type-specific organization of thalamic inhibition in auditory computation.

39 ## INTRODUCTION

40 Inhibition is crucial to sensory information processing and transmission in the brain. In the auditory
41 system, inhibition plays a critical role in shaping auditory computations, from sound localization in the
42 brainstem to statistical inference in the auditory cortex[1–7]. There are many different inhibitory neuron types
43 within the central auditory pathway which differ morphologically, electrophysiologically, and functionally.
44 In auditory cortex, two major sub-classes of inhibitory neurons, parvalbumin- (PV) and somatostatin- (SST)
45 positive neurons, play distinct functional roles[8–16], and activating PV or SST neurons leads to a decrease in
46 frequency selectivity and an overall increase in tone responsiveness of cortical excitatory neurons[10,13,17,18].
47 SST, but not PV, neurons contribute to stimulus-specific adaptation, a phenomenon in which neurons adapt
48 selectively to a subset of inputs presented frequently[8,9,19–23].

49 However, cortical neurons are not the only cells that receive targeted inhibition along the auditory
50 pathway. The medial geniculate body (MGB), located within the thalamus, receives auditory information
51 from the auditory brainstem, and MGB neurons shape and relay sensory information to auditory cortex[24,25].
52 This ascending projection from MGB to auditory cortex is shaped by inhibition from the thalamic reticular
53 nucleus (TRN), a thin sheet of inhibitory neurons that targets and envelops the thalamus[26–30]. Anatomically,
54 the TRN receives excitatory collaterals from the MGB as well as from corticothalamic L5 and L6 neurons,
55 and sends feedforward inhibition back to MGB[27,31–35]. Functionally, the TRN filters relevant sensory
56 information important for perception[36–38] and supports optimal behavioral performance in sensory
57 attentional tasks[39–41].

58 The TRN contains multiple types of inhibitory neurons, predominantly PV and SST positive neurons.
59 Recent findings in TRN subregions dedicated to visual and somatosensory modalities have described
60 segregated distributions of distinct inhibitory neuron subtypes that differentially target distinct thalamic
61 nuclei and exhibit differences in intrinsic and synaptic properties[42–45]. Thus, it is plausible that as a result
62 of both organizational and functional differences, PV^{TRN} and SST^{TRN} neurons might differentially exert
63 inhibitory control of sound processing in the MGB. However, the specific roles of PV^{TRN} and SST^{TRN} neurons
64 in gating the auditory thalamocortical relay have not been systematically tested.

65 In this study, we examined the differential effects of PV^{TRN} and SST^{TRN} neurons on thalamic sound
66 processing. To anatomically identify how PV^{TRN} and SST^{TRN} neurons project to the sub-nuclei of the MGB,
67 we used viral tracing techniques to express an anterograde virus encoding a flexed fluorescent reporter in

68 the TRN of transgenic PV-Cre or SST-Cre mouse lines and traced projections to the MGB. We found that
69 PV^{TRN} and SST^{TRN} neurons target distinct subregions of the MGB. We used viral transfection to drive a soma-
70 targeted inhibitory opsin in the TRN to inactivate PV^{TRN} or SST^{TRN} neurons while recording neuronal activity
71 from neurons in the MGB of awake passively listening head-fixed mice. Inactivating PV cells resulted in a
72 mix of enhanced and suppressed MGB responses. By contrast, inactivating SST cells suppressed the vast
73 majority of MGB responses. To identify candidate circuit mechanisms that could underlie the unexpected
74 bidirectional modulation resulting from inactivation of SST^{TRN} and PV^{TRN} neurons, we examined MGB
75 activity in computational models with varied synaptic connectivity within TRN and from TRN to MGB. These
76 simulations revealed several variations of underappreciated thalamic circuitry that can explain the
77 experimental results, including disynaptic inhibition and divergent inhibition. Together, our results
78 demonstrate cell and circuit specificity of inhibition within the auditory thalamus that is likely to influence
79 auditory perception.
80
81
82 **RESULTS**
83 **PV and SST neurons of the TRN project to MGB, targeting different subregions.**
84 The MGB is anatomically subdivided into three main subnuclei: the ventral division (vMGB), the
85 medial division (mMGB), and the dorsal division (dMGB). vMGB receives lemniscal projections from the
86 brainstem and provides the most direct auditory input to auditory cortex (AC), whereas dorso-medial
87 geniculate regions provide higher-order information. We first imaged the distribution of PV^{TRN} and SST^{TRN}
88 neuronal projections in MGB using viral neuroanatomical tracing methods. We injected anterograde adeno-
89 associated viruses into the TRN of PV-Cre or SST-Cre mice and traced the axonal projections to the MGB
90 (**Figure 1A & 1C**). We took advantage of the finding that calretinin is solely expressed in the higher-order
91 MGB[46] to characterize the projection patterns of both neuronal subtypes within the MGB. We labeled cell
92 bodies in dorso-medial MGB using a calretinin antibody. Whereas PV^{TRN} neurons targeted the central
93 portion of vMGB, SST^{TRN} neurons avoided this region. PV^{TRN} projections were stronger in the central area of
94 ventral MGB rather than peripheral and dorso-medial regions (**Figure 1B;** $N = 14$ ROIs, $p < 0.001$, signed-
95 rank test). By contrast, projections of SST^{TRN} targeted the dorsal and medial MGB (**Figure 1D;** $N = 8$ ROIs,

p = 0.023, signed-rank test). Combined, these data demonstrate that PV^{TRN} and SST^{TRN} neurons exhibit differential projection patterns to the MGB.

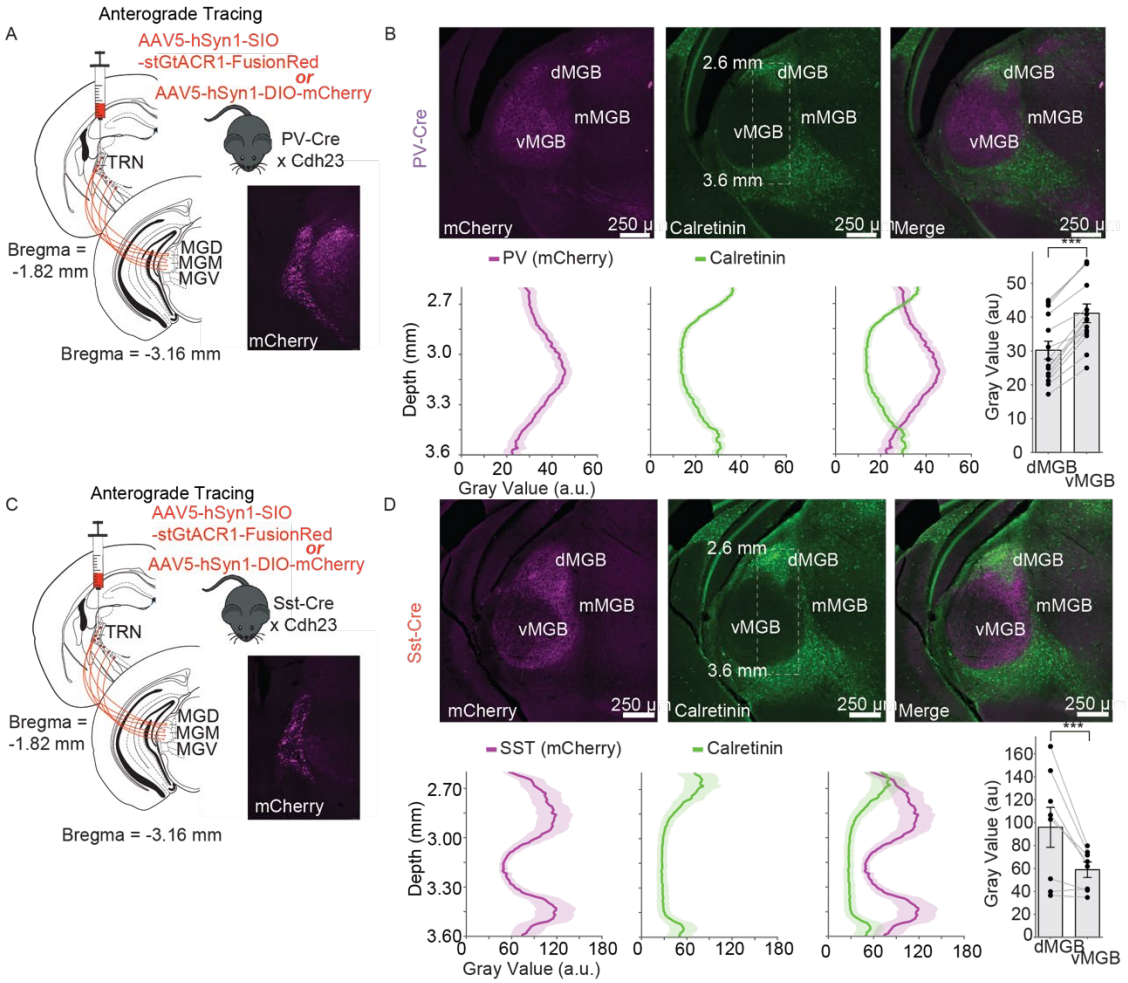

Figure 1. PV^{TRN} and SST^{TRN} project to different subregions of the MGB. A. Experimental design for anatomical experiments. PV-Cre mice were injected with AAV5-hSyn1-DIO-mCherry into TRN for anterograde tracing of PV^{TRN} neurons. Inset: mCherry expression in the TRN indicating the localization of the virus. **B. Top**: Projections of PV^{TRN} neurons primarily target the ventral subdivision of the MGB. *Left panel*: Viral expression of projections to the MGB (magenta). *Middle panel*: Immunohistochemical labeling of calretinin in the MGB (green). *Right panel*: Merged channels. **Bottom**: Quantification of the fluorescence intensity of projections from PV^{TRN} neurons that target MGB (Dashed box in top middle panel outlining the ROI). *Left panel*: intensity of viral expression of projections to the MGB in the ROI along the dorso-ventral axis. Dashed lines indicate extent of vMGB. *Middle panel*: intensity of the immunohistochemical labeling of calretinin in the MGB in the ROI along the dorso-ventral axis. *Right panel*: merged channels. *Bar plot:* mean intensity of the projections of PV^{TRN} neurons in dorsal and ventral MGB (N =14 ROIs; n = 3 mice). **C.** SST-Cre mice were injected with AAV5-hSyn1-DIO-mCherry into TRN for anterograde tracing of SST^{TRN} neurons. **D. Top**: Projections of SST^{TRN} neurons primarily avoid the ventral subdivision of the MGB. *Left panel*: Viral expression of projections to the MGB (magenta). *Middle panel*: Immunohistochemical labeling of calretinin in the MGB (green). *Right panel*: Merged channels. **Bottom**: Quantification of the fluorescence intensity of projections from SST^{TRN} neurons that target MGB (Dashed box in top middle panel outlining the ROI). *Left panel*: intensity of viral expression of projections to the MGB in the ROI along the dorso-ventral axis. *Middle panel*: intensity of the immunohistochemical labeling of calretinin in the MGB in the ROI along the dorso-ventral axis. *Right panel*: merged channels. *Bar plot:* mean intensity of the projections of PV^{TRN} neurons in dorsal and ventral MGB (N = 8 ROIs; n = 3 mice). *Scale bar = 0.25 mm. vMGB: ventral MGB; dMGB:*

120 *dorsal MGB; mMGB: medial MGB; White dashed box in the top middle panel indicates ROI for*
121 *fluorescence intensity quantification.*
122

123 **Inactivation of PV^{TRN} and SST^{TRN} neurons differentially affects tone-evoked responses in the**
124 **MGB.**

125 Motivated by the anatomical distinctions described above and previous work identifying genetically
126 distinct TRN neurons that express different anatomical and physiological properties[42,43], we next tested
127 whether and how sound responses of MGB neurons are modulated by PV^{TRN} and SST^{TRN} inputs. We injected
128 a Cre-dependent soma-targeted inhibitory opsin (AAV5-hSyn-SIO-stGtACR1-FusionRed) into the audTRN
129 of SST-Cre or PV-Cre mice (**Figure 2A-B, 2G-H, Supplementary Figure S1**). This virus only expresses
130 in the soma of Cre-expressing neurons, reducing the chance of effects from backpropagating action
131 potentials from local terminals[47], and because TRN in mice is the only major locus of PV or SST expression
132 close to the injection target, off-target impacts of light are minimized in this experiment. In separate
133 experiments, we verified that the virus expression was restricted to the appropriate cell type
134 (**Supplementary Figure S1**). We then implanted an optic fiber above audTRN, a headpost, and a ground
135 pin for awake *in-vivo* electrophysiological recordings. In our experiments, mice passively listened to 50-ms
136 tones ranging from 3 to 80 kHz (tone-On trials). In some tone-On trials we optogenetically inactivated PV^{TRN}
137 or SST^{TRN} activity simultaneously with the tone (light-On trials), and we also presented light alone (light-
138 Only trials) (**Figure 2A, G**). We recorded and measured the spiking activity of MGB neurons before, during
139 and after tone and/or light presentations. After selecting for neurons that were sound-responsive in the 0-
140 25 ms window after tone onset, we compared firing rates for the light-Off and light-On conditions of tone
141 presentation and identified both significantly facilitated and suppressed MGB responses (**Figure 2B, C, H,**
142 **I**). We then visualized the magnitudes of both types of modulated responses as a function of probe depth
143 within the MGB (**Figure 2D-F, 2J-L**). To confirm that our optogenetic manipulations indeed inhibited
144 audTRN neurons, in a separate set of experiments we tested and found that light stimuli over the TRN
145 suppressed tone-evoked neuronal activity in neurons recorded in TRN (**Supplementary Figure S2**). We
146 also verified that light stimuli suppressed spiking in whole-cell recordings of neurons expressing stGtACR1
147 in slices (**Supplementary Figure S3**).

148 Because TRN is a powerful inhibitor of MGB, we initially expected to find that inactivating TRN
149 neurons would drive disinhibition of sound-driven responses in MGB neurons. We expected this effect to be

150 strongest in central vMGB, the primary sound relay, and mediated by the inhibitory PV^{TRN} neurons that
151 innervate it. Alternatively, because neurons within TRN might be connected by reciprocal inhibition,
152 inactivation of one subset of TRN neurons could disinhibit of another subset of TRN neurons and result in
153 doubled inhibition, or simply, increased suppression of sound responses in MGB.

154 Indeed, inactivating PV^{TRN} neurons facilitated sound-evoked responses in a large fraction of MGB
155 neurons (**Figure 2B, C**). The facilitation was stronger for the ventral regions of MGB than dorsal MGB (p
156 = 0.008, binned by depth: 2.5-2.9 mm versus 3.1-3.5 mm, Mann-Whitney U test), and was exacerbated by
157 the larger number of facilitated neurons in center (**Figure 2D-F**). Surprisingly, there was also a strong
158 suppression of a fraction of neurons throughout MGB. However, this suppression was not differential across
159 the depth of MGB (p = 0.219, Mann-Whitney U test). Inactivating SST^{TRN} neurons resulted in a dominant
160 suppression of tone-evoked responses in MGB, with a handful of neurons exhibiting facilitation (**Figure**
161 **2H, I**). Interestingly, this suppression was also stronger in the dMGB than vMGB (p = 0.012, Mann-Whitney
162 U test) (**Figure 2J-L**). The 4 cells that facilitated were in the v/mMGB (**Figure 2J**). Together with our
163 anatomical results, these findings suggest that PV^{TRN} neurons provide direct inhibition or disinhibition to
164 MGB, while SST^{TRN} neurons predominantly disinhibit the thalamocortical auditory pathway.
165

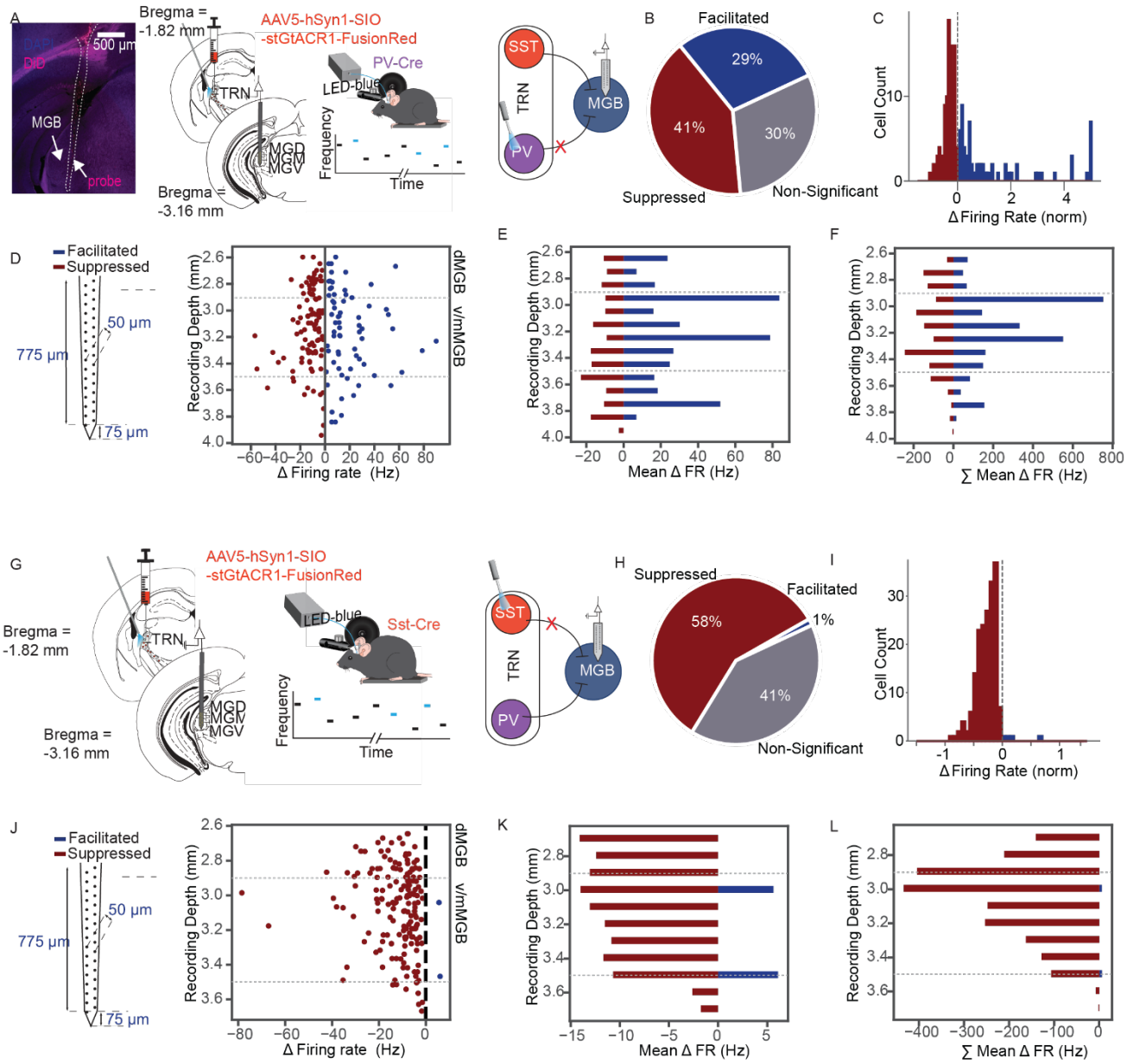

Figure 2. Inactivation of PV^{TRN} and SST^{TRN} neurons differentially affect tone-evoked activity in MGB neurons. A. PV-Cre mice were injected with AAV5-hSyn1-DIO-stGtACR1-FusionRed into the audTRN and were implanted with an optic fiber. We recorded from MGB neurons in awake head-fixed mice. We presented a set of pure tones in light-On and light-Off conditions. We selectively inactivated PV^{TRN} neurons while recording from neurons in the MGB using a vertical multi-channel electrode that spanned the depth of dMGB and vMGB, with the top electrode positioned at the tip of dMGB. Left: Example probe track labeled using DiD (magenta), from a recording in MGB. Center: Images from Paxinos Mouse Brain Atlas with target injection and recording locations superimposed. Right: Diagram of stimuli and recording setup. **B.** Pie chart breaking down the effect of PV^{TRN} inactivation on neurons of the MGB. We found that 41% of recorded units had suppressed tone-evoked responses (red slice), 30% of recorded units had facilitated tone-evoked responses (navy blue slice), and 29% of tone-responsive units were not affected by light manipulation (gray slice). **C.** Distribution of significant modulations of MGB responses during inactivation of PV^{TRN} neurons. Red: suppressed neurons; Blue: facilitated neurons. **D.** Scatter plot showing the change in firing rate (FR) of recorded MGB neurons with PV^{TRN} inactivation as a function of probe depth. Dotted grey lines indicate MGB subregion borders. **E.** Mean change in FR of recorded MGB neurons with PV^{TRN} inactivation as a function of probe depth in 100 mm bins. **F.** Total change in FR of recorded MGB neurons with PV^{TRN} inactivation as a function of probe depth in 100 mm bins. **G-L.** Same as **A- F**, but for SST^{TRN} inactivation,

where we found that 58% of recorded units had suppressed tone-evoked responses (red slice), 1% of recorded units had facilitated tone-evoked responses (navy blue slice), and 41% of tone-responsive units were not affected by SST^{TRN} inactivation (gray slice). (N (PV) = 256, n = 4 mice. N (SST): 312, n = 4 mice). ROIs; n = 3 mice). *Scale bar = 0.50 mm. vMGB: ventral MGB; dMGB: dorsal MGB; mMGB: medial MGB.*

Inactivation of PV^{TRN} neurons facilitates or suppresses tone-evoked responses in MGB.

We next examined in more detail the effect of inactivating PV^{TRN} neurons on tone-evoked responses in MGB. For a representative *facilitated* MGB neuron, the raster plots and peri-stimulus time histogram (PSTH) (**Figure 3A-B**) demonstrate an increase in activity during tone presentation. For this neuron, the increase was most pronounced in the first 25 ms after stimulus onset and affected the responses across tone frequencies (**Figure 3C**). For a representative *suppressed* MGB neuron, the raster plot and PSTH depict a reduction in spiking activity during the tone (**Figure 3D-F**) that was most pronounced in the first 25 ms after tone onset.

Across the population of MGB neurons, PV^{TRN} inactivation during tone presentation resulted in facilitation in 30% of neurons; 41% of neurons were suppressed ,and 29% of neurons in the MGB were not significantly affected by PV^{TRN} inactivation (**Figure 2B, C**). Responses of facilitated neurons demonstrated a sharp peak followed by a prolonged decay in firing rate after tone onset in both light-Off and light-On conditions, and the peak of the tone responses was greater in the presence of light (**Figure 3G**). Response peaks of suppressed neurons to tones followed a similar timecourse but were reduced during light-On relative to tone-On, light-Off trials (**Figure 3H**). When PV^{TRN} neurons were inactivated, time-to-peak significantly increased in facilitated MGB neurons but was unchanged in suppressed MGB neurons (**Figure 3G, H right;** p(facilitated) < 0.05, p(suppressed) = 0.070; signed-rank test), suggesting that PV^{TRN} neurons selectively control dynamics of neuronal responses in MGB.

We verified that over the population, there were no significant differences in spontaneous activity prior to stimuli between the units that were later suppressed or facilitated by PV^{TRN} inactivation during tone presentation (**Figure 3I;** p = 0.856, t-test). Facilitation or suppression of mean tone-evoked firing during the first 25 ms of the tone by inactivation of PV^{TRN} was significant over the population (**Figure 3J**, 0-25 ms post tone onset) and those effects persisted for the duration of the tone (**Figure 3K**, 25-50 ms post tone onset**;** N(facilitated): 74, N(suppressed): 104; p(facilitated) < 0.001, p(suppressed) < 0.001 for both time periods tested; signed-rank test).

To examine whether light responses in MGB – that is, the impacts of inactivating PV^{TRN} -- were affected by the tone, we subtracted the tone responses in the light-On and light-Off conditions. We then compared that difference to baseline-subtracted responses during light-Only (tone-Off) trials. In facilitated neurons, light responses were larger in the tone-On condition than responses to the light-Only (tone-Off) condition (**Figure 3L,** N = 74, p = 0.011). In suppressed neurons, light caused a greater suppression of firing in the tone-ON condition compared to the light-Only condition (**Figure 3M,** N = 104, $p < 0.0001$). These differences in light responses suggest that inhibition provided by PV^{TRN} neurons is supralinear – it is stronger in the presence of tone than in silence and may reflect sound responses of TRN neurons.

We also asked tested whether the effects of PV^{TRN} inactivation differed for MGB recording site(s) that were tonotopically organized along the probe depth (dorsal-ventral axis, increasing best frequency with depth) and those that were not. We found only small differences between the effects of PV^{TRN} inactivation with a slightly greater fraction of neurons suppressed in tonotopic than non-tonotopic sites (**Supplementary Figure S4**).

Overall, these results demonstrate that inactivating PV^{TRN} neurons rapidly and bi-drectionally affected tone-evoked responses in MGB. Thus, PV^{TRN} neurons can both directly suppress neuronal responses in MGB or enhance the response firing rate, thereby involving multiple mechanisms that shape MGB firing rates.

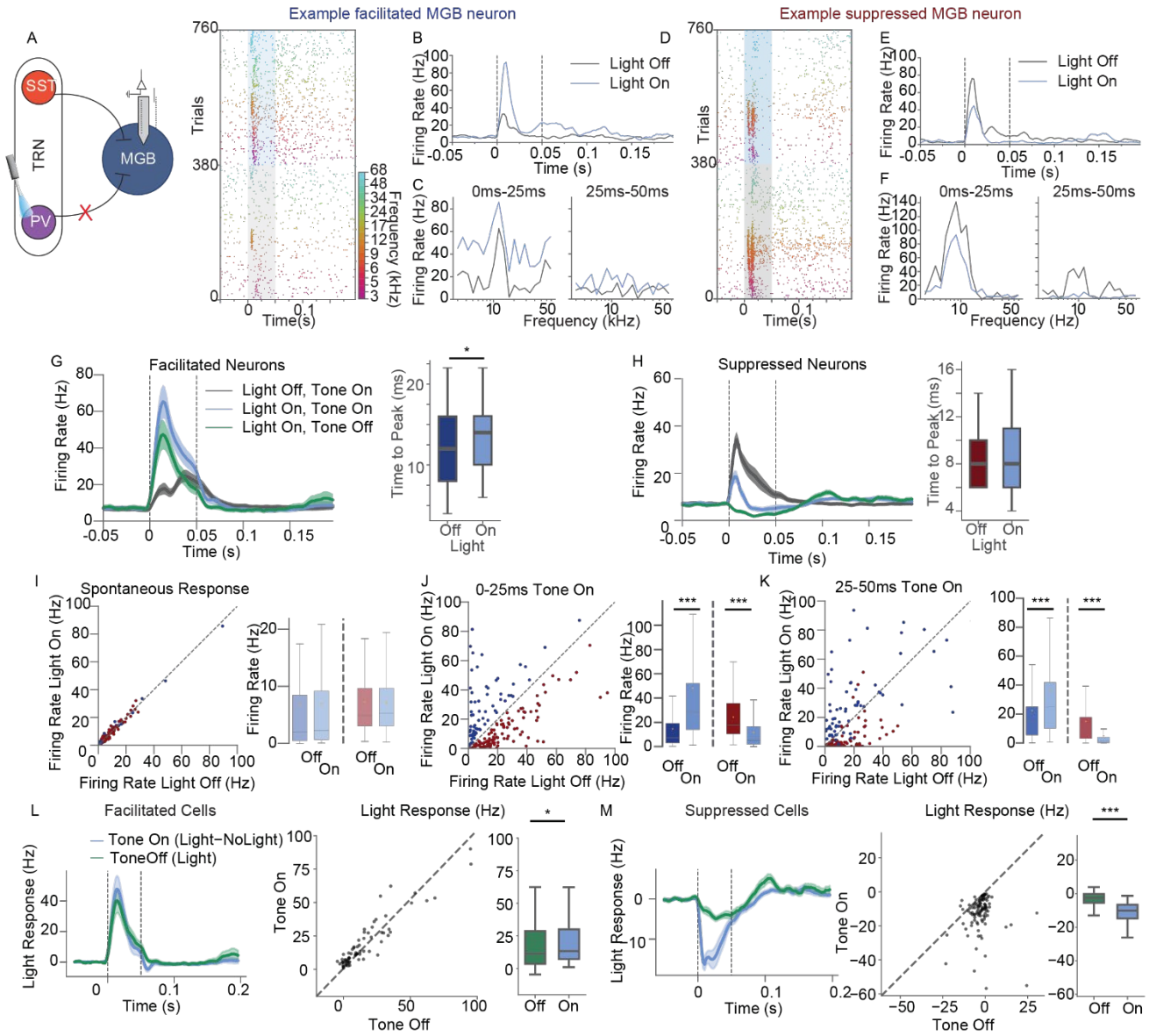

Figure 3. Inactivation of PV^{TRN} neurons facilitates or suppresses tone-evoked activity in MGB neurons. A. PV-Cre mice were injected with AAV5-hSyn1-DIO-stGtACR1-FusionRed into the audTRN and were implanted with an optic fiber. We selectively inactivated PV^{TRN} neurons on half of the trials while recording from MGB neurons in awake head-fixed mice in response to while a pure tones. In light-On trials, light was presented simultaneously with the tone. Raster plot of an example facilitated unit; trials are ordered by frequency and light condition. The gray box indicates light-Off conditions, and the blue box indicates the light-On conditions. **B.** PSTH of the facilitated example unit averaged across all trials for light-Off (black line) and light-On (blue line) conditions. **C.** Frequency response function for the facilitated unit during the early and late 25 ms of tone presentation during light-Off and light-On conditions. **D-F.** same as A-C, but for a representative suppressed neuron. **G, H.** Left: Mean PSTH of facilitated (G) and suppressed (H) recorded neurons in MGB (N = 74 facilitated and N = 104 suppressed neurons) for Light-Only trials (green line), tone-On, light-Off trials (black line), and tone-On, light-On trials (light blue line). Right: Times to peak of tone-evoked responses for facilitated (G, blue) and suppressed H, red) MGB neurons for light-Off (blue/red) and light-On (light blue) trials. **I-K.** Left: scatter plots and box plots of the firing rates for light-Off and light-On conditions for facilitated (blue) and suppressed (red) neurons during spontaneous activity prior to tone/light presentation (**I**), 0-25 ms post tone onset (**J**), and 25-50 ms post tone onset (**K**). **L, M.** Left panels: baseline-subtracted light responses for light-Only stimuli (green) , and light-induced change in firing rate between the two tone-On conditions (blue, difference between tone-On, light-On and tone-On, light-Off firing rates). Middle panel: scatter plot, and right panel: Box plots of mean firing rate changes in

light response in tone-On vs. tone-Off conditions for the first 0-25 ms of stimulus presentation. **L:** facilitated neurons. **M:** suppressed neurons. Dashed line is x = y. *N = 256 units; n = 4 mice. Here and below, boxplots depict the median and interquartile range (IQR) for each condition; whiskers extend to values within 1.5xIQR; shaded areas in psths represent SEM±; error bars represent SEM±. *** denotes p-value < 0.001; * denotes p-value < 0.05.*

Inactivation of SST^{TRN} neurons primarily suppresses tone-evoked responses of MGB neurons.

We next examined in more detail the effect of inactivating SST^{TRN} neurons on tone-evoked responses of MGB neurons. For a representative *facilitated* MGB neuron, the raster plots and post-stimulus time histograms (**Figure 4A-B**) demonstrate an increase in activity at the onset of tone presentation. For this neuron, the increase was present in the first 25 ms after stimulus onset and affected the responses to frequencies near the neuron's best frequency (**Figure 4C**). For a representative *suppressed* MGB neuron, the raster plot and PSTH depict a reduction in spiking activity throughout the tone (**Figure 4D, E**). The suppressive effects were most pronounced in the first 25 ms after tone onset (**Figure 4F**).

Across the population of neurons, during tone presentation and SST^{TRN} inactivation 58% neurons were suppressed, only 1% of neurons were facilitated and 41% of neurons in the MGB were not affected by SST^{TRN} inactivation (**Figure 2H, I**). The average PSTH across the few facilitated neurons (N = 4 neurons) shows a small increase in firing during light presentation (**Figure 4G**). Suppression driven by SST^{TRN} neuronal inactivation followed a similar timecourse as the effects of PV^{TRN} inactivation (**Figure 4H**). There was no change in the time-to-peak response of the 4 facilitated MGB neurons, and no change for time to peak in suppressed MGB neurons, upon inactivation of SST^{TRN} neurons (**Figure 4G, H right;** p(facilitated) = 1.0, p(suppressed) = 0.071; signed-rank test).

We verified that over the population, there were no significant differences in spontaneous activity prior to stimuli across units that were later suppressed or facilitated by SST^{TRN} inactivation during tone presentation (**Figure 4I;** p = 0.458, t-test). In neurons classified as suppressed, neuronal activity was significantly reduced by SST^{TRN} inactivation during the tone presentation for both the first 25 ms (**Figure 4J**) and the second 25 ms (**Figure 4K**) of tone presentations, while changes in the small set of facilitated neurons were not significant as a group (**Figure J, K;** N(suppressed): 181, N(facilitated): 4; p(facilitated) =0.125, p(suppressed) < 0.001 for both time windows; signed-rank test). We found that SST^{TRN} inactivation suppressed a greater fraction of neurons in non-tonotopically than in tonotopically organized recording

282 sites, suggesting that the disinhibition provided by SST^{TRN} neurons may be localized to non-lemniscal MGB
283 subdivisions consistent with our anatomical findings (**Supplementary Figure S5**).

284 To examine whether light responses in MGB – that is, the impacts of inactivating SST^{TRN} -- were
285 affected by the tone, we compared the baseline-subtracted light-Only response to the difference in tone-On
286 responses during light-On and light-Off trials. The response to the light was increased during the tone in the
287 few facilitated neurons in comparison to the light-only response (**Figure 4L**, $N = 4$, $p = 0.026$), and
288 decreased in suppressed neurons (**Figure 4M,** $N = 181$, $p < 0.0001$), again suggesting a supralinear effect
289 of SST inhibition during tone presentation and possible contributions from sound responses of TRN
290 neurons. Overall, these results demonstrate that inactivating SST^{TRN} neurons largely drives suppression of
291 MGB neurons.

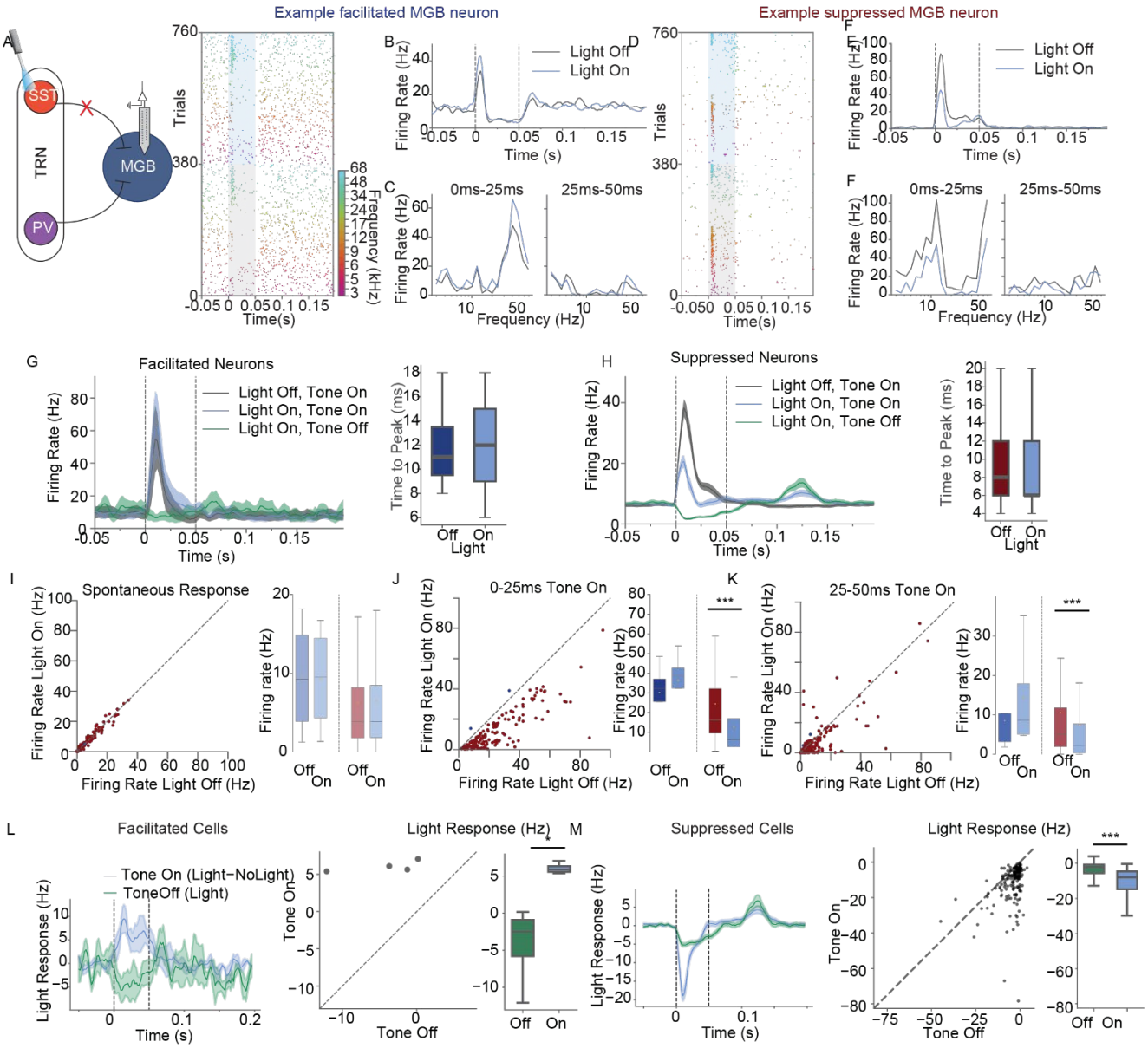

Figure 4. Inactivation of SST^{TRN} neurons predominantly suppresses tone-evoked activity in MGB neurons. A. SST-Cre mice were injected with AAV5-hSyn1-DIO-stGtACR1-FusionRed into the audTRN and were implanted with an optic fiber. We recorded from MGB neurons in awake head-fixed mice. We presented a set of pure tones in light-On and light-Off conditions. Light was simultaneous with the tone. We selectively inactivated SST^{TRN} neurons while recording from neurons in MGB. Raster plot of an example facilitated unit; trials are ordered by frequency and light condition. The gray box indicates light-Off conditions, and the blue box indicates light-On conditions. **B.** PSTH of the facilitated example unit averaged across all trials for the light-Off (black line) and light-On (blue line) conditions. **C.** Frequency response function for the facilitated unit during the early and late 25 ms of tone presentation during light-Off and light-On conditions. **D-F.** same as A-C, but for a representative suppressed neuron. **G, H.** Left: Mean PSTH of facilitated (G) and suppressed (H) recorded neurons in MGB (N = 4 facilitated. N = 181 suppressed) for light-Only trials (green line), tone-On, light-Off trials (black line), and tone-On, light-On trials (light blue line). Right: Time to peak of tone-evoked responses for facilitated (G, blue) and suppressed (H, red) MGB neurons for light-Off (blue/red) and light-On (light blue) trials. **I-K.** Scatter plots and box plots of mean firing rates for light-Off and light-On conditions for facilitated (blue) and suppressed (red) neurons during spontaneous activity (**I**), 0-25 ms post stimulus onset (**J**), and 25-50 ms post stimulus onset (**K**). **L, M.** Left panels: baseline-subtracted light responses for light-Only stimuli (green), and light-induced change in firing rate between the two tone-On conditions (blue, difference between tone-On, light-On and tone-On, light-Off firing rates). Center: scatter plot of firing rate changes in light response in tone-On vs. tone-Off

conditions. Right: box plot of mean light responses in tone-Off and tone-On conditions. Dashed line is x = y. **L:** Facilitated neurons. **M:** Suppressed neurons. *N = 312 units; n = 4 mice.*

PV^{TRN} and SST^{TRN} differentially affect frequency tuning of MGB neurons.

Inactivation of PV^{TRN} neurons produced significant changes in MGB frequency tuning for both the facilitated- and suppressed- <GB neuronal populations, with a significant shift upwards and a significant shift downwards in the frequency response functions, respectively (**Figure 5A-B;** N(facilitated): 74, N(suppressed): 104; p(facilitated-all octaves) < 0.001, p(suppressed-all octaves) < 0.001; signed-rank test). To examine frequency selectivity of neurons (or how specific neuronal responses are to a best frequency) we calculated the sparseness index across the responses. In the sparseness index, a value close to 1 indicates that units respond more selectively to a preferred stimulus or central frequency, whereas a value close to 0 indicates that units respond to a broader range of stimuli or frequencies. We found that inactivation of PV^{TRN} significantly affected sparseness in both facilitated and suppressed subgroups. Following PV^{TRN} inactivation, sparseness in facilitated MGB neurons significantly decreased, indicating that neurons became more broadly responsive (**Figure 5A;** p < 0.001; signed-rank test). Interestingly, in suppressed MGB neurons, PV^{TRN} inactivation increased sparseness, indicating that neurons on average became more narrowly responsive (**Figure 5B;** p < 0.001; signed-rank test). These results indicate that PV^{TRN} neurons contribute to how narrowly or broadly tuned MGB neurons are to auditory stimuli.

Inhibition of SST^{TRN} neurons produced no significant changes in tuning for the few MGB neurons that had facilitated tone-evoked responses (**Figure 5C;** N (facilitated): 4; p > 0.1; signed-rank test). However, in the MGB neurons suppressed by SST^{TRN} inactivation, firing rates showed a significant downward shift in the frequency response function (**Figure 5D;** N = (suppressed): 181; p < 0.001; signed-rank test). Inactivation of SST^{TRN} neurons did not affect sparseness in the small facilitated group *(***Figure 5C***; N* (facilitated): 4; p = 0.125; signed-rank test). However, similar to PV^{TRN} inactivation, sparseness in suppressed MGB neurons increased significantly during SST^{TRN} inactivation (**Figure 5D;** N (suppressed): 181; p < 0.001; signed-rank test).

We also examined whether the best frequency and tuning width for frequency-tuned MGB neurons changed during PV^{TRN} or SST^{TRN} inactivation. To do this, we fit a Gaussian function to each MGB neuron tuning curve in both the light-On and light-Off conditions (examples, **Supplementary Figure 6 D, H, L**) and compared the standard deviation σ parameter, which corresponds to the width of frequency tuning. In

342 line with our findings that PV^{TRN} and SST^{TRN} inactivation increased sparseness in suppressed MGB neurons,
343 MGB neurons that were suppressed by PV^{TRN} inactivation showed a significant decrease in σ (PV:
344 **Supplementary Figure S6 F, G**, N = 26, t = 2.42, p = 0.027; SST: **Supplementary Figure S6 J, K,** N
345 = 47, t = 3.30, p = 0.0002). However, for neurons facilitated by PV^{TRN} inactivation, there was no change in
346 σ between light-On and light-Off conditions (**Supplementary Figure S6 A, B,** N = 11, t = -1.27, p = 0.278)
347 and there were no well-fit facilitated neurons during SST^{TRN} inactivation. Together, these results suggest
348 that changes in MGB response sparseness may at least partially be due to changes in the width of frequency
349 response function evoked by manipulation of TRN inhibitory neurons.

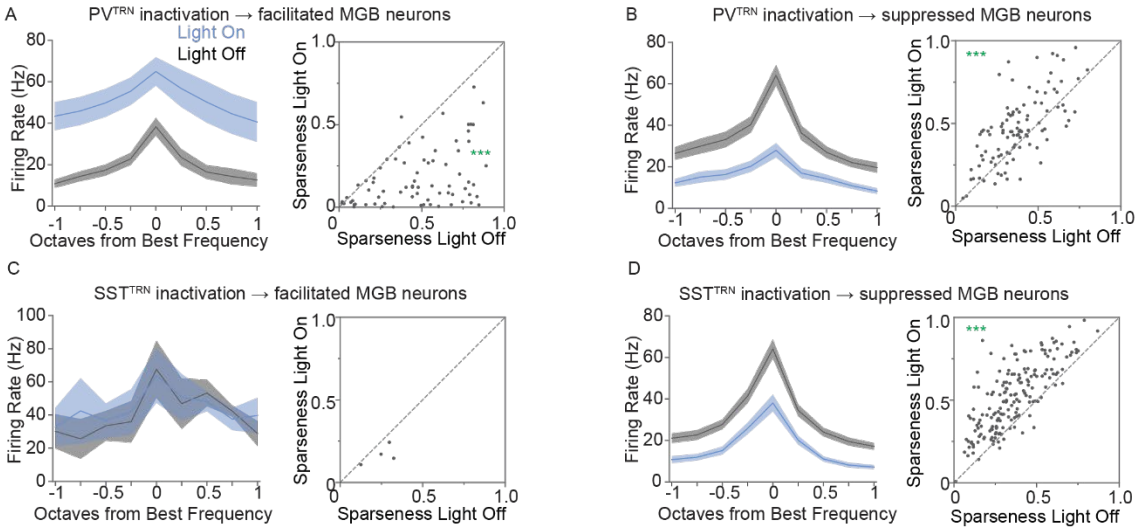

350

351 **Figure 5. Inactivation of PV^{TRN} and SST^{TRN} neurons differentially affect frequency tuning of**
352 **MGB neurons. A-D.** *Left:* Mean frequency response functions for light-On (light blue) and light-Off (light
353 gray) trials for neurons, centered on best frequency (BF = 0 octaves). Shaded areas represent SEM±. *Right.*
354 Scatter plots of sparseness for light-On versus light-Off conditions. **A, C.** Facilitated neurons. **B, D.**
355 Suppressed neurons. *N = 256 neurons; n = 4 mice (PV). N = 312 neurons; n =4 mice (SST). *** denotes p-*
356 *value < 0.001; * denotes p-value < 0.05.*
357
358 **Specifics of connectivity between MGB-TRN circuits determine the sign of MGB responses**
359 **during TRN cell-type inactivation.**
360
361 To examine the many possible connectivity schemes of primary and higher-order auditory
362 thalamocortical circuits that may account for the observed changes in sensory responses during inactivation
363 of specific TRN populations, we constructed a 4-cell Hodgkin-Huxley model (see Methods) comprising two
364 channels: a primary vMGB relay cell reciprocally connected to a PV^{TRN} cell, and a higher-order MGB cell
365 reciprocally connected to a SST^{TRN} cell (**Figure 6A-B**), matching the subtype-specific connections that we
366 identified and have been previously demonstrated for other sensory modalities[42,43]. Without connectivity

367 between primary and higher-order channels, inactivation of the PV^{TRN} cell always allowed substantially
368 increased responses in the vMGB firing rate to a tone input, whereas inhibiting the SST^{TRN} cell has no effect
369 at all on vMGB response, as expected (not shown). Those trials served as a comparison control for
370 subsequent trials.

371 We first examined whether intra-TRN connectivity would suffice to produce both suppression and
372 facilitation of vMGB responses during cell type-specific silencing (**Figures 3,4**). Electrical synapses
373 extensively couple TRN cells, including coupling between subtypes[45], that may substantially modulate
374 activity within the thalamocortical circuits examined here[48,49]. We examined the effect of inter-type TRN
375 coupling, using a strong electrical synapse with coupling coefficient ~0.2, on the responses of the primary
376 MGB cell. Similar to the uncoupled control case, vMGB responses were facilitated when PV^{TRN} was
377 inactivated (**Figure 6D**, left), and once again as expected we saw no changes in vMGB responses during
378 inactivation of SST^{TRN} (**Figure 6D, right**). Although the existence of inhibitory synapses between TRN
379 neurons in mature tissue has been controversial [50], there is some evidence for lateral inhibition within
380 TRN[51,52]. Inclusion of a lateral inhibitory synapse from SST^{TRN} to PV^{TRN} allowed for facilitated vMGB
381 response during PV^{TRN} inactivation, and we noted that MGB responses during no-inactivation trials were
382 also elevated from the control response (**Figure 6E, left**). Silencing SST^{TRN} cells in this circuit produced a
383 substantial reduction in the tone response of the vMGB neuron compared to control responses (**Figure 6E,**
384 **right**), matching the experimental results (**Figure 2, 4**) through relief of disynaptic inhibition. We also
385 noted changes in the spontaneous rates for light-Only trials during subtype silencing that was consistent
386 with the experimental recordings (**Figure 6E, cyan lines**). Silencing either of the cell types in a circuit that
387 included inhibitory connections from PV^{TRN} to SST^{TRN} did not reduce tone responses of vMGB, however (not
388 shown). Thus, one specific form of intra-TRN connectivity, from SST^{TRN} to PV^{TRN} cells, is a candidate circuit
389 mechanism underlying the unexpected suppression of MGB during cell type-specific TRN inactivation.

390 Next, we asked whether the responses of primary vMGB change during cell type-specific inactivation
391 in the context of variations in feedback inhibition. TRN cells send divergent inhibitory connections to several
392 MGB cells but do not often send inhibition back to the same cells that excite them[53,54]. Additionally,
393 activation of one thalamic nucleus can produce inhibition in nearby sensory-related nuclei (i.e. activation of
394 POM evoking IPSCs at VPM) thought to arise from the TRN[55,56]. Thus, we included and varied the amount
395 of divergent feedback inhibition from the TRN to the MGB in our circuits. In circuits with only divergent but

396 lacking reciprocal inhibitory feedback, PV^{TRN} inactivation produced a suppression of vMGB responses
397 (**Figure 6F, left**), while SST^{TRN} inactivation produced facilitation of vMGB responses (**Figure 6F, right**).
398 In circuits with only divergent inhibitory feedback as well as a lateral SST^{TRN} to PV^{TRN} connection, PV^{TRN}
399 inactivation produced a suppression of vMGB responses (**Figure 6G, left**), while SST^{TRN} inactivation
400 produced greater facilitation of vMGB responses (**Figure 6G, right**). Thus, we conclude that uniformly
401 divergent feedback inhibition is unlikely to account for the experimental observations of vMGB suppression
402 during SST^{TRN} inactivation.

403 As we anticipate that spectrums of inhibitory connectivity and strength may co-exist in live tissue,
404 we then asked whether the relative strengths of within-TRN, lateral inhibition and TRN-MGB reciprocal
405 inhibition could control the sign of vMGB responses during selective silencing. To test the effect of
406 heterogeneous circuitry on firing rate changes in primary vMGB cells, we varied the ratio of lateralization
407 within the modeled circuits over sets of trials. In circuits where TRN and MGB were reciprocally connected,
408 varied relative strengths of lateral intra-TRN inhibition always produced facilitation of vMGB responses
409 when PV^{TRN} was inactivated (**Figure 6H, left**); the effect of SST^{TRN} lateralization was only to modulate the
410 total facilitation produced. During SST^{TRN} inactivation, increases in SST^{TRN} lateral inhibition suppressed
411 MGB responses independently of the presence of PV^{TRN} lateral inhibitory synapses (**Figure 6H, top right**).
412 We note that the addition of coupling between TRN cells allowed for bidirectionality in changes in vMGB
413 rate when SST^{TRN} was inactivated for networks with weak SST-to-PV lateralization (**Figure 6H, bottom**
414 **right**). From this set of simulations addressing intra-TRN connectivity, we conclude that inactivating
415 SST^{TRN} can reproduce the unexpected suppression of vMGB responses when SST-to-PV synapses or gap
416 junctions are included in the circuit; however, these lateral intra-TRN connections alone cannot reproduce
417 the bidirectional effects of PV^{TRN} inactivation.

418 Finally, we asked if variations in the relative power of the two types of feedback inhibition, combined,
419 could allow both vMGB enhancement and suppression during cell type-specific inactivation trials.
420 Increasing the relative strength of the divergent inhibitory synapses decreased the responses of the vMGB
421 cell, while increasing the strength of reciprocal inhibition increased those responses, during PV^{TRN}
422 inactivation trials compared to the baseline firing rate (**Figure 6I, top left**). This is consistent with the
423 bidirectionality of the experimental results for PV^{TRN} inactivation (**Figure 3**). SST^{TRN} inactivation produced
424 only increases in vMGB activity, as divergent inhibitory ratio increased from zero (**Figure 6I, top left**),

inconsistent with experiments. However, electrical coupling added to this circuitry allowed SST^{TRN} inactivation to diminish vMGB responses for weakly lateralized networks (**Figure 6I, middle**). Including SST^{TRN}-to-PV^{TRN} lateral inhibition in this case modulated the SST^{TRN} inactivation response towards more suppressed outcomes (**Figure 6I, bottom right).** Together, our simulations lead us to conclude that divergent feedback connections, together with electrical synapses or SST^{TRN}-to-PV^{TRN} inhibition, may be embedded within the thalamus and serve as the sources of the bidirectional vMGB responses observed during PV^{TRN} inactivation and the suppression during SST^{TRN} inactivation.

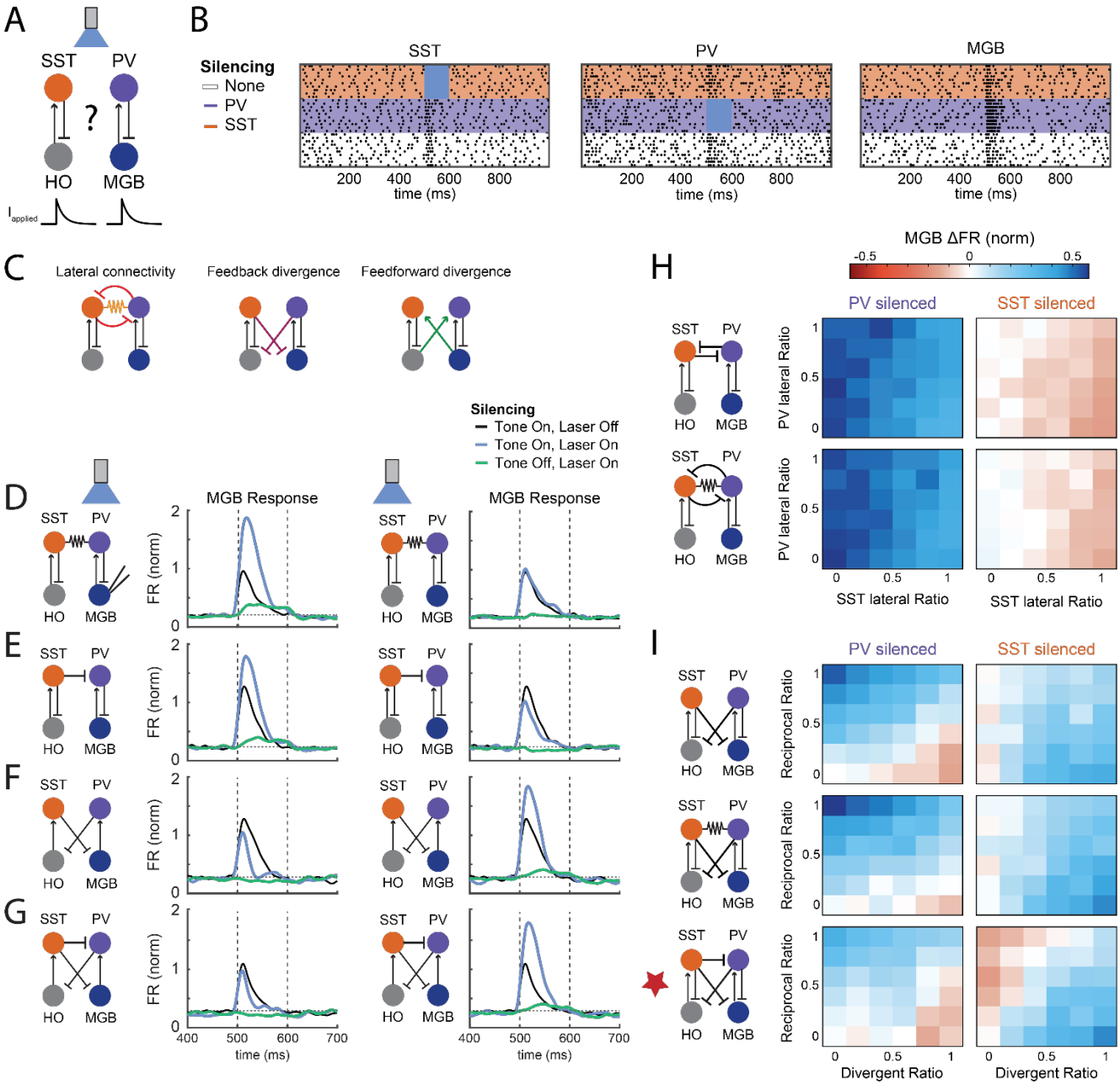

Figure 6. Schemes of circuit connectivity that account for bidirectional modulation of vMGB responses during subtype-specific inactivation in TRN. A. 4-cell model of primary sensory MGB-TRN pairs and higher order (HO) MGB-TRN pairs. **B.** Raster plots from trials with no inactivation, during PV inactivation (purple) and during SST^{TRN} inactivation (orange). **C.** Candidate connectivity schemes tested in models. **D.** PSTH of

MGB firing for circuits with electrical coupling between TRN subtypes. MGB responses are normalized to the peak response during non-inactivated trials with no connectivity between columns. Left, primary MGB firing rate to input alone (black line) and with PV^{TRN} silencing (light blue line). Right, MGB firing rate input alone (black line) and with SST^{TRN} silencing (light blue line). **E**. As in D, for a circuit including lateral SST^{TRN} to PV^{TRN} connections. **F**. Effect of inactivation on MGB rate for heterogeneous combinations of lateral inhibitory connections, with and without electrical synapses between TRN cells. The ratio of lateral synapses is the percent of trials that included lateral synapses for each TRN cell type. **G.** As in D, for circuits with both reciprocal and divergent feedback inhibition. **H.** As in D, for circuits containing only divergent inhibition. **I.** Effect of cell type-specific inactivation on MGB rates for heterogeneous inhibitory feedback connections between TRN and thalamic cells. Divergence ratio is the percent of trials that included divergent synapses. Reciprocal ratio is the percent of trials that included reciprocal TRN-MGB synapses. Middle, with electrical coupling between PV and SST cells. Bottom, effects of TRN inactivation on MGB rate with heterogeneous inhibitory connections in addition to lateral inhibition from the SST^{TRN} to PV^{TRN} cells.

DISCUSSION

Differences between intrinsic physiology, synaptic connections, and axonal projections of distinct cell types have been described for the GABAergic neurons of the TRN[42–45], but the impact of those differences on their inhibitory modulation of thalamic processing remains unknown. We used a combination of viral anatomical tracing, optogenetics, awake *in-vivo* electrophysiological recording, and computational modeling to study the functional roles of audTRN PV and SST neurons in modulating sound responses in the MGB. Our results confirm that audTRN PV and SST neurons project to hierarchically distinct sensory thalamic regions: while PV^{TRN} neurons primarily project to the center of the primary or first-order auditory thalamic sub-region vMGB, SST^{TRN} neurons project almost exclusively to the dorsal subregions of MGB and higher-order auditory thalamus (**Figure 1**). Here, we performed recordings in awake mice to examine the effects of audTRN PV and SST neuron inactivation on the intact auditory circuit. We found that inactivating these distinct subpopulations of audTRN inhibitory neurons had diverging effects on auditory tone responses of MGB neurons **(Figure 2)**. While inactivation of PV^{TRN} neurons facilitated a large fraction of MGB neurons, we also found that inactivation of both PV^{TRN} and SST^{TRN} neurons suppressed a large fraction of responses in MGB (**Figures 2, 3, 4**). Our results show that inactivation of both PV^{TRN} and SST^{TRN} neurons altered the frequency tuning responses of MGB neurons **(Figure 5, S6)**. In addition, computational models allowed us to identify several embedded variations of circuitry between TRN and MGB that could enable the experimental observations (**Figure 6,** for summary see **Figure 7**).

Together, our anatomical, electrophysiological, and simulation results indicate complex roles for TRN inhibition on MGB neurons and suggest a larger degree of divergence than what has been suggested from the anatomical work here and by others[42,43]. A variety of connection schemes have been proposed for TRN, including intra-TRN inhibition[51,51], lack of intra-TRN inhibition[50], typed reciprocal inhibition[42,43], and

open-loop or divergent connectivity to thalamic nuclei[55,56]. Cross-modal TRN responses have also been reported[57,58], offering further evidence of nuanced connectivity. In addition, gap junctions of the TRN could be exclusive within one set or both sets of cell types or modality, or promiscuous across types[45], or absent in adult tissue. Our computational survey of these possibilities suggests that divergence of TRN-MGB connectivity is necessary, in addition to reciprocal inhibition, to achieve the bidirectional responses in MGB observed for PV inactivation; and that some intra-TRN connectivity, whether gap junctional and/or GABAergic, plays a role in allowing for the suppressive effects of SST inactivation. Our modeling offers several predictions for future experiments using optogenetic approaches. First, our model predicts a cell-specific inhibitory connection from SST^{TRN} to PV^{TRN}. Second, divergent inhibition (*e.g.* from SST^{TRN} to vMGB neurons) could also be evaluated in the same experiment. Moreover, our modeling predicts that SST^{TRN} are driven by higher order cells; thus inactivating the higher order population while also inactivating the SST^{TRN} would potentially reverse the observed impact on vMGB responses during SST silencing. Similar experiments in future studies could be applied to test a PV^{TRN}-d/mMGB connection.

One proposed mechanism for our results is the possibility of intra-TRN synapses between PV^{TRN} and SST^{TRN} neurons, similar to the interactions in cortical regions[1]. Evidence for GABAergic synapses between nearby TRN neurons in slice preparations is exceedingly sparse[50,59], but longer-range intra-TRN interactions are possible, and reports of dendro-dendritic synapses have been reported in the TRN of the cat[60]. Driven by our modeling results, our subsequent experiments found one example of such a connection in slice recordings (**Supplementary Figure S7**). It has also been reported that excitatory collateral inputs from thalamic relay nuclei drive excitatory input onto TRN neurons and therefore activate TRN neurons[61]. It is also possible that the suppression effects in tone-responsive units of the MGB is a direct result of fast feedback arising from excitatory MGB collaterals, intra-TRN dendro-dendritic synapses, or other regions of GABAergic inputs to the TRN like the basal forebrain, substantia nigra or lateral hypothalamus[62–65].

While our experiments did not include a behavioral component, our results have clear implications for modulation from the TRN during active behaviors. Our results suggest that PV^{TRN} and SST^{TRN} neurons may play distinct roles in behaviors that rely on lemniscal or non-lemniscal thalamic function. The TRN receives diverse modulatory inputs, including projections from the substantia nigra reticulata[64], the basal forebrain[65–67], globus pallidus[68–70] and hypothalamus[63]. Whether these inputs are cell type-specific is unknown. Our results indicate that the impact of inhibiting or modulating specific TRN neuron types is

complex and raises interest in the types, sources, and targets of modulatory input to the thalamocortical pathways, along with the function of these projections. For example, inhibition of specific classes of TRN neurons that results in specific suppression or facilitation of the thalamocortical relay could be a mechanism for modulating sensory perception in line with behavioral state. Indeed, recent studies have shown the contributions of MGB to associative behavior memory tasks[71].

Our experiments and analyses do not account for the feedback provided to MGB and TRN from the cortex. Within the auditory thalamus, the TRN provides the majority of inhibition to the MGB, however, MGB neurons also receive feedback from corticothalamic neurons in L5/L6 of AC as well as input from other association areas, such as the BLA[33,72,73]. It is possible that the suppressive effects we observed included a component of fast feedback inhibition from another region of the brain, or polysynaptic interactions. Future studies using high-density channel probes to record from multiple brain areas simultaneously could further our understanding of inhibitory circuit mechanisms. For example, recording from the TRN-MGB-AC circuit simultaneously while optogenetically manipulating 1) corticothalamic feedback, 2) TRN-MGB inhibitory synapses, or 3) collateral inputs from MGB to the TRN would allow for recording effects of audTRN on neural responses along the auditory pathway. An extensive anatomical tracing study would also specifically identify possible sources of GABAergic input to the PV^{TRN} and SST^{TRN} neurons involved in the auditory pathway. This could reveal possible sources of feedback inhibitory inputs to the TRN that might drive the tone-evoked suppression we observe in our study. In addition, descending cortical projections to the TRN are tonotopic, and this organization may result in PV^{TRN} and SST^{TRN} inhibition of the thalamocortical relay that is not only anatomically structured but also frequency specific. Future studies could examine how optogenetic inhibition of different frequency regions of auditory cortex alters the firing of PV^{TRN} and SST^{TRN} neurons, and the resulting changes in MGB neuron tuning curves.

Additionally, the role of the TRN in integrating sound information across the two ears remains to be investigated. In our study, viral injections and electrophysiological recordings were performed contralateral to the position of the speaker. Neurons in the MGB are biased toward the contralateral ear, and sound intensity from the freestanding speaker is stronger at the contralateral ear as opposed to the ipsilateral ear; therefore, we expected that the sound emitted by the speaker would predominantly drive neurons in the recorded location[74]. Nonetheless, sound still reaches the ear that is contralateral to the speaker, and that information is transferred to the contralateral superior olive and eventually the contralateral MGB (relative

530 to the speaker) [75]. Additionally, neurons in the MGB receive inputs from both ipsi- and contralateral IC[76]. In
531 parallel, information about the sound is processed within the ipsilateral MGB relative to the speaker and
532 inhibition from that ipsilateral TRN may affect processing in the contralateral MGB via direct or indirect
533 projections. To disentangle these effects, future experiments may include reversible ear-plugging of the
534 contralateral ear, bilateral neuronal modulations or simply varying the speaker position.

535 Combined, our results provide an insight into the complexity of the audTRN and identify cell-type
536 specific mechanisms for controlling sound processing in the auditory thalamus.

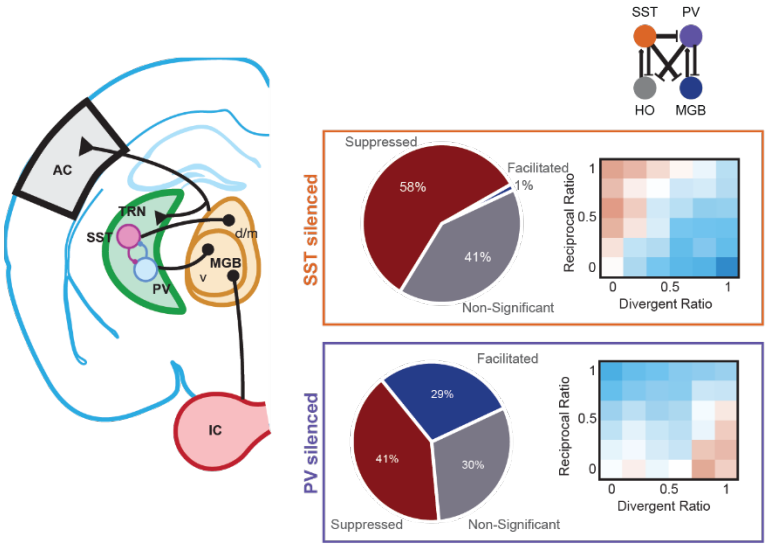

537

538 **Figure 7. Inhibitory neurons differentially control sound-evoked responses in the MGB.** Left:
539 diagram of the proposed circuit underlying our results. Boxes: summary of effects of optogenetic
540 manipulation of SST^{TRN} or PV^{TRN} inactivation on MGB firing and the circuitry and results of computational
541 models that support a similar distribution of effects.
542

543 ## MATERIALS AND METHODS

544 *Animals.*

545 We performed all experimental procedures in accordance with NIH guidelines on use and care of
546 laboratory animals and by approval of the Institutional Animal Care and Use Committee at the University
547 of Pennsylvania (protocol number 803266). Care was taken to minimize any pain, discomfort, or distress of
548 the animals during and following experiments. Experiments were performed in adult male (n = 12) and
549 female (n = 12) mice aged 3-8 months and weighing 20-32g. The mouse lines used in this study were crosses
550 between Cdh23 mice (B6.CAST-Cdh23^{Ahl+}/Kjn; RRID:IMSR_JAX:002756)—a transgenic line that has a
551 targeted point reversion in the Cdh23 gene which protects mice from age-related hearing loss[77]—and PV-
552 Cre mice (B6.129P2-Pvalb$^{tm1(cre)Arbr}$/J; RRID:IMSR_JAX:017320) or SST-Cre mice (SST$^{tm2.1(cre)Zjh}$/J;

553 RRID:IMSR_JAX:013044). Mice were housed at 28°C on a reversed 12hr light-dark cycle with ad libitum
554 access to food and water. Experiments were performed during the animals' dark cycle and housed
555 individually in an enriched environment after major surgery. Euthanasia was performed by infusion of a
556 ketamine (300mg/kg) and dexmedetomidine (3mg/kg) or prolonged exposure to CO_2. Both methods are
557 consistent with the recommendations of the American Veterinary Medical Association (AVMA) Guidelines
558 on Euthanasia.
559
560 *Surgical Procedures.*
561 Mice were induced to a surgical plane of anesthesia with 3% isoflurane in oxygen and secured in the
562 nose cone of a stereotaxic frame. Animals were then maintained in an anesthetic plane with 1-2% isoflurane
563 in oxygen and kept at a body temperature of 36° C with the use of a homeothermic blanket. Prior to any
564 surgical procedure, mice were administered subcutaneous injections of sustained release buprenorphine (1
565 mg/kg) for analgesia, dexamethasone (0.2 mg/kg) for reduction of swelling, and bupivacaine (2 mg/kg), for
566 local anesthesia. Mice received a subcutaneous injection of an antibiotic, enrofloxacin (Baytril; 5 mg/kg), for
567 3 days as part of their post-operative care.
568
569 *Viral Injections.*
570 Approximately 21 days prior to electrophysiological recordings or transcardial perfusions, we
571 performed small (0.5 mm in diameter) unilateral craniotomies using a micromotor drill (Foredom)–under
572 aseptic conditions–over auditory TRN (audTRN) or MGB. Glass syringes attached to a syringe pump (Pump
573 11 Elite, Harvard Apparatus) were backfilled with modified viral vectors, placed over the brain region of
574 interest, and used to inject virus at 60 nL/min. Glass syringes were made using a micropipette puller (P-97,
575 Sutter Instruments) from glass capillaries (Harvard Apparatus, 30-0038) with tip openings ranging from
576 30 -40 μm in diameter. Following injections, syringes were left in place for 15-20 min before retraction.
577 Craniotomies were then covered with bone wax (Fine Science Tools) or a removable silicone plug (Kwik-
578 Cast, World Precision Instruments). The coordinates used to target audTRN were: -1.80 mm posterior to
579 bregma, ±2.25 mm lateral to bregma, -2.90 mm below the pial surface. The MGB coordinates used were: -
580 3.30 mm posterior to bregma, ±2.00 mm lateral to bregma, -2.90 mm below the pial surface.
581

582 *Viral Vectors.*

583 For soma-targeted inactivation of PV or SST neurons of the audTRN we injected 400 nL of AAV5-hSyn1-
584 SIO-stGtACR1-FusionRed (≥7×10^{12} vg/mL, Addgene 105678-AAV5). For anterograde tracing of PV or SST
585 neurons of the audTRN and control experiments we injected 400-450 nL of AAV5- hSyn-DIO-mCherry (≥
586 7×10^{12} vg/mL, Addgene 50459-AAV5).

587

588 *Fiber Optic Cannula & Headpost Implantation.*

589 Following virus injections, fiber optic cannulas (Prizmatix: 3 mm in length, 1.25 mm in diameter, Ø
590 200 µm core, 0.66 NA) were implanted above audTRN at a 20° angle, -1.80 mm posterior to bregma, ±3.25
591 mm lateral to bregma, and -2.50 mm below the pial surface. A small craniotomy was made over the left
592 frontal lobe and a ground pin was implanted. Craniotomies were sealed with Kwik-Cast (World Precision
593 Instruments). The cannula, ground pin and a custom-made stainless-steel headpost (eMachine shop) were
594 then secured with dental cement (C&B Metabond, Parkell) and dental acrylic (Lang Dental).

595

596 *Tissue Processing.*

597 After allowing time for proper viral expression or following electrophysiological recordings, mice
598 were deeply anesthetized with a cocktail of ketamine and dexmedetomidine (*see Animals*) and transcardially
599 perfused with 1X PBS followed by 4% paraformaldehyde (PFA) in PBS. Brains were extracted and post-fixed
600 in 4% PFA overnight at 4° C. Following post-fixation, tissue was cryoprotected in 30% sucrose for at least
601 24 h at 4° C until sectioning. Brain sections 40-50 µm in thickness were cut on a cryostat (Leica CM1860)
602 and collected for immunohistochemistry or imaging of viral expression. For imaging of viral expression or
603 probe location, 50 µm sections were mounted on gelatin-coated glass slides and coverslipped using ProLong
604 Diamond Antifade Mounting media with DAPI (Invitrogen P36971). For immunohistochemistry, 40 µm
605 sections were collected in 12-well plates filled with 1X PBS (5-10 sections per well). Slides were imaged using
606 a fluorescent microscope (Leica DM6 B) or a confocal microscope (Zeiss LSM 800).

607

608 *Immunohistochemistry.*

609 Free-floating 40 µm-thick brain sections were first washed in 1X PBS (3 x 10 min washes). To
610 increase membrane permeability, sections were microwaved for approximately 10 s and then incubated in a

611 solution of 0.3% Triton X-100 in 1X PBS (hereinafter referred to as PBT) for 30 min at room temperature.
612 The sections were then incubated in a blocking solution consisting of 5% normal goat serum in PBT
613 (hereinafter referred to as PBTG) for 0.5-1 h at room temperature. Following incubation with PBTG, sections
614 were incubated in primary antibody solution which consisted of the following antibodies diluted in PBTG:
615 (1) 1:500 mouse monoclonal anti-Parvalbumin (Swant, PV-235; RRID:AB_10000343), (2) 1:500 rabbit
616 polyclonal anti-Somatostatin (Immunostar, 20067); RRID: AB_572264), and (3) 1:1000 rabbit polyclonal
617 anti-Calretinin (Swant, Calretinin-7697; RRID:AB_2721226). Incubation in primary solution was done
618 overnight-48 h at 4° C on a shaker plate (Fisher Scientific); well plates were covered with parafilm and a
619 plastic lid. Following incubation with primary antibody solution, sections were washed in PBT (3 x 10 min
620 washes). Sections were then incubated in secondary antibodies conjugated to fluorescent markers diluted in
621 PBTG for 2 h at room temperature; well plates were covered with aluminum foil to block light. Secondary
622 antibodies used were: (1) for PV staining, Alexa Fluor Plus 488 Goat anti-Mouse IgG (H+L) (Invitrogen
623 A32723; RRID: AB_2633275), (2) for SST staining, Alexa Fluor Plus 488 Goat anti-Rat IgG (H+L)
624 (Invitrogen A48262; RRID: AB_2896330), and (2) for Calretinin staining, Alexa Fluor Plus 488 Goat anti-
625 Rabbit IgG (H+L) (Invitrogen A32731; RRID: AB_2633280). Sections were then incubated for 10 min in a
626 1:40,000 dilution of DAPI stock solution in PBT (5 mg/mL, Invitrogen D1306). The sections were
627 subsequently washed in 1X PBS (5 x 10 min washes). Sections were then mounted on gelatin-coated glass
628 slides, coverslipped using ProLong Diamond Antifade Mounting media (Invitrogen P36970) and left to
629 curate in the dark, on a flat surface at room temperature for at least 24 h prior to imaging. Slides were imaged
630 using a fluorescence microscope (Leica DM6 B) or a confocal microscope (Zeiss LSM 800).
631
632 *Acoustic Stimuli.*
633 Stimuli were generated using custom MATLAB code and were sampled at 200 kHz with 32-bit
634 resolution. Acoustic stimuli were delivered through a speaker (Newark Multicomp, MCPCT-G5100-4139)
635 positioned in the direction of the animals' ear contralateral to the recording site. To test for stimulus-locked
636 auditory responses, we used a set of click trains made up of 5 broadband noise bursts at a rate of 1 Hz. The
637 noise bursts were 25 ms long and presented at a rate of 10 Hz for a total of 500 ms. To assess frequency
638 response functions in neuronal populations, we generated a set of 19 pure tones of logarithmically spaced
639 frequencies ranging between 3 kHz and 80 kHz at 70 dB sound pressure level relative to 20 μPa (SPL). Each

640 tone was 50 ms long with a 1-ms cosine squared ramp, repeated 40 times with an inter-stimulus-interval of
641 300 ms and presented in a pseudo-random order. 20 of those 40 tone repetitions were accompanied by a
642 continuous light pulse with a 1-ms cosine squared ramp starting at tone onset and ending at tone offset (50
643 ms; for details on light stimuli see Optogenetic Inactivation).
644
645 *Optogenetic Inactivation and Calibration.*
646 To inactivate populations of TRN neurons, we injected a soma-targeted inhibitory opsin in the
647 audTRN of PV- and SST-Cre mice (see Viral Injections and Viral Vectors). On light-Only trials, we delivered
648 continuous (1-ms cosine squared ramp) light pulses of different durations (10 ms, 25 ms, 50 ms, and 100
649 ms) through an implanted fiber-optic cannula via a fiber-coupled blue LED (460 nm, Prizmatix,
650 Optogenetics-LED-Blue). During sound presentation, on light-On trials, we delivered a continuous 50-ms
651 pulse with a 1-ms squared ramp concurrent with the tone stimulus.
652 To reduce variability in the effects of optogenetic manipulation across mice, we developed a
653 procedure to calibrate the LED intensity prior to each recording session. Once the probe was in its final
654 depth for recording, we presented alternating click trains (*see Acoustic Stimuli*) where each trial consisted
655 of a click train without LED stimulation, followed by a click train paired with LED stimuli with one of 20
656 intensities (LED driving voltage ranged from 0 to 5 V) while recording neural responses. This stimulus set
657 was presented 10 times for each intensity value. Neural responses were sorted offline using Kilosort2. To
658 calculate if each unit was significantly sound responsive and discard noise clusters, we computed a Wilcoxon
659 sign-rank test between sound responses during the light-Off click trains and a baseline period of activity. We
660 excluded any units with P-values exceeding a Bonferroni-corrected α-level of $0.05/n_{clusters}$ from further
661 analysis. We then calculated the number of spikes during the light-Off click train trials (n_{OFF}) and during
662 the light-On click train trials (n_{ON}) and computed the percent change in the response (r_{PC}) for each light
663 intensity:

664 $$r_{PC} = \frac{n_{ON} - n_{OFF}}{n_{OFF}} * 100$$

665 Using a logistic function, we fit the response function as a function of the LED voltage,

666 $$y = a + \frac{b}{1 + e^{-(x-c)d}}$$

667 where a determines the y-offset of the response, b determines the range of the response, c determines the x-
668 offset, and d determines the gain of the response. With this fit equation, we determined the voltage value
669 driving the LED that elicited a 100% increase (2-fold change) in neural response and we used that voltage
670 for all subsequent LED stimuli presented in each individual recording session (0.1-5 mW). Some sessions
671 did not produce a 2-fold increase with LED manipulation; for these sessions we used maximum LED power
672 (5 mW) for all stimuli.
673
674 *Acute Electrophysiological Recordings.*
675 All electrophysiological recordings were carried out in a double-walled acoustic-isolation booth
676 (Industrial Acoustics). At least 21 days following viral injection, animals were anesthetized (see Surgical
677 Procedures) and a small craniotomy (1 mm in diameter) was performed using a micromotor drill (Foredom)
678 over MGB (for coordinates see Viral Injections). Mice were then clamped into a custom base and allowed to
679 recover from anesthesia for at least 30 min. Following recovery, we vertically (0° on stereotaxic arm) lowered
680 a 32-channel silicon probe (NeuroNexus: A1x32-Poly2-10mm-50s-177) to a depth of ~3.5 mm from the pial
681 surface using a motorized micromanipulator (Scientifica) attached to a stereotaxic arm (Kopf) at a rate of 1-
682 2 μm/s. While we lowered the probe, a train of brief broadband noise clicks was played (*see Acoustic*
683 *Stimuli*). If we observed stimulus-locked responses, we determined the probe was in a sound-responsive
684 area. After some recordings, the probe was coated with a lipophilic far-red dye (Vybrant DiD, Invitrogen)
685 and lowered in the recording location to determine recording sites (*see Tissue Processing*; **Figure 2C**).
686 Recordings that did not display stimulus-locked responses post-hoc were not used for further analysis. Once
687 the probe reached the target recording depth, it was left to settle in the brain for at least 30 min prior to
688 recording. Neural signals were amplified via an Intan headstage (RHD 32ch, Intan Technologies), recorded
689 at a rate of 30 kHz using an OpenEphys acquisition board and GUI[78], and digitized with an SPI cable. Signals
690 were filtered between 500 and 6000 Hz, offset corrected, and re-referenced to the median of all active
691 channels. Recorded neural data were spike sorted using KiloSort2[79] and manually corrected using phy2.
692 Upon manual correction, units were classified as either single- or multi- units; if units exhibited a clear
693 refractory period they were labeled single units, otherwise they were classified as multi-units. We later tested
694 the proportions of single- and multi-units that were inhibited, facilitated or unchanged by SST and PV
695 inactivation and found no differences between the groups (**Supplementary Figure S8**); therefore both

696 single and multi-units were included in subsequent analyses (for number of units used see **Table 1**).
697 Approximately 3 recording sessions were acquired from each individual mouse at different recording sites.
698 For analysis in **Supplementary Figure S4**, we fit linear fit to recordings depth versus best frequency of
699 neurons for each session, and designated sessions with a positive slope and significant p value ($p < 0.05$) as
700 tonotopic, whereas other recording sites were designated as non-tonotopic [80,81].
701
702 *Gray Value Analysis & Cell Counting*.
703 *Gray Value:* We first delineated the MGB across the different ROIs. We then used the Fiji Plot Profile
704 plugin to quantify gray values. We used a custom Python script to calculate the mean gray values and S.E.M.
705 *Cell Counting:* We used the Cellpose[82] anatomical segmentation algorithm to outline cells in selected
706 sections. We then manually confirmed the masks provided by Cellpose in Fiji using the cell counter plugin.
707 A custom Python script was used to calculate the overlapping masks and percentages.
708
709 *Neural Response Analysis*.
710 We selected units for further analysis for inclusion based on their stimulus response profiles. We
711 repeated experiments after injecting a virus encoding only the fluorescent reporter without an opsin and
712 found no significant effect of light on neuronal responses 0-25 ms after tone onset, but a mixed effect of light
713 on responses 25-50 ms and 50-75 ms after tone onset: no effect for PV-Cre mice, but a significant effect in
714 SST-Cre mice (**Supplementary Figures S9, S10**). This effect likely corresponds to delayed visual
715 responses and may be due to leakage of light between the skull and the fiberoptic cannula. Therefore, we
716 focused our main analyses on responses 0-25 ms after tone onset. To select sound- and light- responsive
717 units, we fit an ordinary least square linear regression model to mean responses on each trial during 0-25
718 ms after the sound onset with sound and light as predictors and a (light x sound) interaction predictor. We
719 selected units that had significant sound predictor as sound-responsive; and units that were significant for
720 light responses as those with significant light or light-sound interaction predictors ($\alpha < 0.05$). Spontaneous
721 firing rate was computed as the average firing rate during the 25 ms prior to tone onset for light-Off and
722 light-On trials separately. Tone-evoked firing rate was calculated as the average firing rate for the first 25
723 ms of the total tone duration for light-Off and light-On trials separately. For some figures, we also computed
724 the firing rates in the late (25-50 ms) and offset (50-75 ms) periods after tone onset. Light-Only responses

725 were calculated as the average firing rate for the first 25 ms of light-Only trials. We calculated differences
726 between responses in light-On and light-Off conditions by subtracting the mean of the firing rates during
727 the first 25 ms of tone presentation in the light-On trials from that in light-Off trials: light-responsive cells
728 with positive difference were classified as facilitated, and with negative difference as suppressed. To
729 calculate frequency response functions, we averaged the firing rate during the first 25 ms of tone
730 presentation for each trial of the 19 frequencies tested in both light-Off and light-On conditions. Best
731 frequency was defined as the frequency that elicited the largest change in firing rate compared to baseline
732 activity. Sparseness for each neuron was calculated separately for the light-Off and light-On conditions
733 during the first 25 ms of tone presentation. The sparseness equation used is as follows:

734 $$s = \frac{1 - \frac{(\sum_i r_i /N)^2}{\sum_i r_i^2 /N}}{1 - 1/N}$$

735 where r_i is the firing rate of a single neuron at each frequency and N is the number of frequencies tested. To
736 examine how frequency tuning changes in light-On and light-Off conditions (**Supplementary Figure S6**),
737 we fit a Gaussian curve of the form

738 $$f(x) = a \cdot e^{-\frac{1}{2}\left(\frac{x-\mu}{\sigma}\right)^2} + baseline$$

739 to the mean frequency response function of each unit. We initialized each fit four times using different initial
740 parameters, calculated R^2, and selected the fit that explained the highest amount of variance in the data
741 (highest R^2).

742

743 *Statistical Analysis.*

744 We used ordinary least squares regression with light and tone as factors to assay for significant effect
745 on individual neuronal responses over trials, as well as for significance of their interactions using ols function
746 in Python. We assessed normality of the data using a Shapiro-Wilk tests using Scipy's Stats Python Library.
747 For paired data that violated the assumption of normality, p values were calculated using a Wilcoxon sign-
748 rank tests using Scipy's Stats Python Library. For non-paired data that violated the assumption of normality,
749 p values were calculated using a Wilcoxon rank-sum tests using Scipy's Stats Python Library. The standard
750 error of the mean was used to calculate error bars (± SEM). Symbols: * indicates p values <0.05, ** indicates
751 p values < 0.01, and *** indicates p values <0.001.

752

753 *Computational Modeling*.

754 Model cells were Hodgkin-Huxley formalism solved by a second order Runge-Kutta ODE solver in
755 MATLAB (ode23, Mathworks). TRN and MGB cells were single-compartment Hodgkin-Huxley models built
756 upon those used previously [48,83,84] that include T currents. To match the reduced bursting properties in
757 SST^{TRN} and higher-order MGB cells[43,85], those cells had 50% reduced T current densities (0.375 mS/cm^2).
758 Parameters included the following ionic currents and maximal conductances: fast transient Na+ (NaT) 60.5
759 mS/cm^2, K+ delayed rectifier (Kd) 60 mS/cm^2, K+ transient A (Kt) 5 mS/cm^2, slowly inactivating K+ (K2)
760 0.5 mS/cm^2, slow anomalous rectifier (AR) 0.025 mS/cm^2, and low threshold transient Ca2+ (CaT) 0.75
761 mS/cm^2 for PV/MGB cells and 0.375 mS/cm^2 for SST/HO cells. Reversal potentials were 50 mV for sodium,
762 -100 mV for potassium, 125 mV for calcium, -40 mV for AR and -75 mV for leak. Capacitance was 1 μF/cm^2
763 with leak of 0.1 mS/cm^2. Chemical synapses were modelled as double exponential decay with rise and fall
764 time kinetics of 5 ms and 35 ms respectively, with reversal potentials of 0 mV for excitatory and -100 mV for
765 inhibitory synapses. Electrical synapses were modelled as static coupling conductance of 0.03 mS/cm^2
766 applied to the voltage difference between the coupled TRN cells, corresponding to a strong electrical
767 coupling (~0.2 coupling coefficient). Tone inputs were simulated as exponentially decaying current pulses
768 (peak amplitude 2.7 μA/cm^2, with decay time constant 30 ms) delivered simultaneously to each of the MGB
769 cells. Each of the TRN cells was inactivated individually through a static conductance of 10 mS/cm^2 and
770 reversal potential of -70 mV for 100 ms during the inputs (**Figure 7B**). Chemical synaptic connections
771 between TRN cells were set at 1 μA/cm^2 for excitatory synapses from MGB to TRN cells, and 3 μA/cm^2 for
772 all inhibitory synapses originating from TRN. For each stimulus condition, we repeated 150 trials under
773 Poisson random noise of 0.2 μA at a rate of 80 Hz for excitatory and 20 Hz for inhibitory events. Among
774 these trials, we varied the percent of trials that included various synaptic connections from TRN cells
775 (**Figure 7C**), in lieu of varying synaptic strengths. Subthreshold current steps of 0.3 μA were applied to all
776 cells to increase excitability. PSTHs were obtained from spike time data histograms with a bin size of 1 ms
777 and smoothed with a 31 ms Hanning window. We normalized each response to the maximum rate in the
778 non-inactivated trial.

779

780 ## RESOURCE AVAILABILITY

781 ### Lead Contact

782 Further information and requests for resources and reagents should be directed to and will be
783 fulfilled by the Lead Contact, Maria Geffen (mgeffen@pennmedicine.upenn.edu).
784

785 ### Data & Code availability

786 Source data has been deposited in Dryad: https://doi.org/10.5061/dryad.ht76hdrq5. Data analysis
787 code is available on GitHub: https://github.com/geffenlab/Rolon_Martinez_2024. Code for the model is
788 available at github: https://github.com/jhaaslab/TRN_MGB_celltypespecific.
789

790 ### Acknowledgements

791 The authors would like to thank the members of the Geffen and Haas laboratories and Yale Cohen for their
792 discussions and helpful comments.
793

794 ### Financial Disclosure

795 This work was supported by the following grants from NIH: R01DC15527, R01DC014479, R03DC013660
796 to MNG, F31DC018473 to SRM, F31DC016524to CFA, from NINDS R01NS113241 to MNG and R01
797 NS128713 to JSH. The funders had no role in study design, data collection and analysis, decision to
798 publish, or preparation of the manuscript.
799

800 ### Supplementary Figure Legends.

801
802 **Supplementary Figure S1. Co-expression of PV+ and SST+ neurons with the inhibitory soma**
803 **targeted opsin stGtACR1.FusionRed. A.** *Left*: AAV5.hSyn.SIO.stGtACR1.FusionRed expression in the
804 audTRN of a PV-Cre mouse. *Middle*: Immunohistochemical expression of parvalbumin-positive neurons.
805 *Right*: Merged image of PV-audTRN neurons expressing both the parvalbumin antibody and the inhibitory
806 opsin. **B**. Quantification of PV+ neurons, PV+stGtACR1.FusionRed+ neurons, and stGtACR1.FusionRed+
807 neurons. **C.** *Left*: AAV5.hSyn.SIO.stGtACR1.FusionRed expression in the audTRN of an SST-Cre mouse.
808 *Middle*: Immunohistochemical expression of somatostatin-positive neurons. *Right*: Merged image of SST-
809 audTRN neurons expressing both the somatostatin antibody and the inhibitory opsin. **D**. Quantification of
810 SST+ neurons, SST+stGtACR1.FusionRed+ neurons, and stGtACR1.FusionRed+ neurons. *Scale bar =*
811 *100μm. Arrows represent example cells. N=2 mice for each group.*
812
813 **Supplementary Figure S2. Optical inactivation of SST^{TRN} neurons suppresses tone-evoked**
814 **activity in the TRN. A.** Average firing rate of recorded units in the TRN in response to 50 ms tone, with
815 vs without optical inactivation of SST neurons (AAV5-hSyn1-SIO-stGtACR1-FusionRed in SST-cre mouse).
816 n= 27 units. Shaded areas represent SEM±. **B.** Average firing rates of TRN units during baseline (Spont),
817 tone-evoked responses (Tone) and offset responses (Offset), with vs without optical inactivation of SST
818 neurons. ***p<0.001, Wilcoxon signed-rank tests. Error bars represent SEM±. **C.** Average firing rate (FR)
819 of TRN units in response to tones on light ON versus light Off trials (with and without optical inactivation
820 of SST neurons). ***p<0.001, Wilcoxon signed-rank test. **E.** Average frequency response function of TRN
821 units with vs without optical inactivation of SST neurons. ***p<0.001, **p<0.01, *p<0.05, Wilcoxon signed-
822 rank tests

Supplementary Figure S3. A. Overlay of live IR and fluorescence images of slice from PV-Cre mouse injected with AAV5_hSyn1-SIO-stGtACR1-FusionRed. **B.** Whole-cell recordings from a TRN neuron from (A) expressing GtACR1, injected with varying amplitudes of current (bottom) and exposed to widefield LED stimulation (blue bar). V_m = -80 mV. Scale bar 25 mV, 250 ms. *Methods for Supplementary Figure S3: 400* nL of AAV5_hSyn1-SIO-stGtACR1-FusionRed was injected to TRN (-2 AP, 1.35 ML, 3.0 and 3.2 depth; Kopf) of PV-Cre (Jax: 017320) animals under sterile anesthetized surgery. Mice were transcardially perfused with NMDG ACSF solution (in mM): 92 NMDG, 2.5 KCl, 1.25 NaH_2PO_4, 30 $NaHCO_3$, 20 HEPES, 25 glucose, 2 thiourea, 5 NA ascorbate, 3 NA pyruvate, 0.5 $CaCl_2$, and 10 $MgSO_4{\cdot}7H_2O$ (315 mOsm L–1, 7.3-7.4 pH). Horizontal brain slices 250 µm thick were cut and incubated in NMDG solution. Slices were incubated at 34°C for 12-15 min in NMDG following cutting and returned to HEPES ACSF at room temperature until recording. The HEPES ACSF solution comprised in mM: 92 NaCl, 2.5 KCl, 1.25 NaH_2PO_4, 30 $NaHCO_3$, 20 HEPES, 25 glucose, 2 Thiourea, Na ascorbate, NA pyruvate, 2 $CaCl_2$, and 2 $MgSO_4{\cdot}7H_20$ (315 mOsm L–1, 7.3-7.4 pH). The ACSF bath during recording contained (in mM): 126 NaCl, 3 KCl, 1.25 NaH_2PO_4, 2 $MgSO_4$, 26 $NaHCO_3$, 10 dextrose, and 2 $CaCl_2$ (315–320 mOsm L–1, saturated with 95% O2/5% CO_2). The submersion recording chamber was held at 34°C (TC-324B, Warner Instruments). Electrodes were filled with (in mM): 135 potassium gluconate, 2 KCl, 4 NaCl, 10 Hepes, 0.2 EGTA, 4 ATP-Mg, 0.3 GTP-Tris, and 10 phosphocreatine-Tris (pH 7.25, 295 mOsm L^{-1}). 1 M KOH was used to adjust pH of the internal solution. The approximate bath flowrate was 2 ml min^{-1} and the recording chamber held approximately 5 ml solution. TRN was visualized under 4x magnification, and TRN cells from auditory sector were identified and patched under 40x IR-DIC optics (SliceScope, Scientifica, Uckfield, UK). GtACR was excited by a 472 nm diode delivered through the objective (CoolLED pE-300). Voltage signals were amplified and low-pass filtered at 8 kHz (MultiClamp, Axon Instruments, Molecular Devices, Sunnyvale, CA,USA), digitized at 20 kHz with custom Matlab routines controlling a National Instruments (Austin, TX, USA, USB6221 DAQ board), and data were stored for offline analysis in Matlab (Mathworks, R2018b, Natick, MA, USA). Recordings were made in whole-cell current-clamp mode. Pipette resistances were 5-9 MΩ before bridge balance; recordings were discarded if access resistance exceeded 25 MΩ.

Supplementary Figure S4. Similar tone and optogenetic responses for recorded MGB neurons in tonotopic and non-tonotopic recording sites in PV-cre mice. A. Plot of neurons' best frequency vs. recording depth for tonotopic recording sites; N= 47 neurons, 2 recording sites, 2 mice. Red line shows linear regression; r = .41, p = .0047. **B.** Pie chart breaking down the effect of PV^{TRN} inactivation in tonotopic recordings. N= 14 suppressed neurons (49%), 23 facilitated neurons (30%), 10 non-significant neurons (21%). **C, D.** Mean PSTH of facilitated (C) and suppressed (D) recorded neurons in MGB. Light-only trials (green line), tone-only trials (black line), and tone- and laser-on trials (light blue line). Shaded areas represent SEM±. **E-H.** Same as A-F, but for non-tonotopic recording sites. **G.** N= 209 neurons, 10 recording sites, 3 mice; r=-0.06, p=0.39. **H.** N= 81 suppressed neurons (39%), 60 facilitated neurons (29%), 68 non-significant neurons (33%).

Supplementary Figure S5. Greater proportion of light-modulated MGB neurons in non-tonotopic than tonotopic recording sites during SST inactivation. A. Plot of neurons' best frequency vs recording depth for tonotopic recording sites; N= 39 neurons, 1 recording sites, 1 mouse. Red line shows linear regression; r = .67, p = 3e-6. **B.** Pie chart breaking down the effect of SST^{TRN} inactivation in tonotopic recordings. N= 2 facilitated neurons (5%), 8 suppressed neurons (21%), 29 non-significant neurons (74%). **C,D.** Mean PSTH of facilitated (E) and suppressed (F) recorded neurons in MGB. Light-only trials (green line), tone-only trials (black line), and tone- and laser-on trials (light blue line). Shaded areas represent SEM±. **E-H.** Same as A-F, but for non-tonotopic recording sites. **G.** N= 273 neurons, 9 recording sites, 4 mice; r=0.062, p=0.31. **H.** N= 173 suppressed neurons (63%), 2 facilitated neurons (1%), 98 non-significant neurons (36%).

Supplementary Figure S6. Inactivation of PV^{TRN} and SST^{TRN} neurons shapes frequency tuning in MGB neurons. A. scatterplot of μ for light-On and light-Off conditions for neurons facilitated by PV^{TRN} inactivation (first row) and neurons suppressed by PV^{TRN} inactivation (second row). **B.** Scatterplots of σ for light-On and light-Off conditions. **C.** Mean frequency response function for light-On (light blue) and light-Off (light gray) trials for neurons centered on μ (0 octaves = μ). **D.** A sample tuning curve for light-On (light blue) and light-Off (grey) conditions along with the gaussian fit for each curve. E-H. Sams as A-D, for suppressed MGB neurons during PV^{TRN} inactivation. **I-L.** Same as *A-D* for SST^{TRN} inactivation, suppressed MGB neurons. Facilitated neurons not show because only N = 1 neuronal responses were well-fitted by a Gaussian for both light on and light off conditions.

We first evaluated how well each tuning curve fit a Gaussian function in both the light-On and light-Off conditions (see Methods). We found that overall the number of MGB neurons with good Gaussian fits (R^2 > 0.6 and μ/σ within tested range) was greater in the light-Off condition (n = 33/74 facilitated units and 58/104 suppressed units during PV^{TRN} inactivation; n = 84/181 suppressed units during SST^{TRN} inactivation) compared to the light-On condition (19/74 facilitated units and 43/104 suppressed units during PV^{TRN} inactivation; n = 88/181 suppressed neurons during SST^{TRN} inactivation) in all groups, except for neurons facilitated by SST^{TRN} activation (light-Off, n = 1/4 neurons, light-On, n = 1/4 neurons).

We found no differences in μ (best frequency) for neurons that had good fits in both light-On and light-Off conditions. We did not find significant differences between groups (units facilitated during PV^{TRN} inactivation: N = 11, t = 0.94, p = 0.37; units suppressed during PV^{TRN} inactivation: N = 26, t = 1.36, p = 0.186; units suppressed during SST^{TRN} inactivation: N = 47, t = -1.47, p = 0.147). MGB neurons that were suppressed by PV^{TRN} inactivation showed a significant decrease in σ (PV: N = 26, t = 2.42, p = 0.027; SST: N = 47, t = 3.30, p = 0.0002). However, for neurons facilitated by PV^{TRN} inactivation, there was no change in σ between light-On and light-Off conditions (N = 11, t = -1.27, p = 0.278) and there were no well-fit facilitated neurons during SST^{TRN} inactivation.

Supplementary Figure S7. Optogenetic identification of TRN^{SST} to TRN^{nonSST} inhibitory synapse. A. Widefield image of brain slice containing TRN from an SST-Cre mouse injected with AAV9-DIO-stChrome-mRuby. **B.** 40x image from A with patched neuron; no mRuby expression in this field. **C.** mRuby expression in another field from A confirming neuronal expression. **D.** Inward responses (IPSCs) from neuron patched with high-Cl^- internal solution following widefield optogenetic excitation (red bar). Scale bar 30 pA, 10 ms. Traces are offset for clarity. **E.** Peak-aligned average of responses from D. Scale bar 10 pA, 10 ms. Decay of the IPSC was best fit by a dual exponential with time constants 3.9 and 275 ms. **F.** Latencies of IPSCs from D.

Supplementary Figure S8. Proportion of facilitated and suppressed MGB single units and multi-units. A. Proportion of MGB MUA clusters (left) and single units (right) that were facilitated, suppressed, and non-significantly modulated by PV^{TRN} inactivation. **B**. Proportion of MGB MUA clusters (left) and single units (right) that were facilitated, suppressed, and non-significantly modulated by SST^{TRN} inactivation.

913 **Supplementary Figure S9. Control experiments for optogenetic manipulation of PV^{TRN}**
914 **neurons. A.** PV mice were injected with an AAV5-hSyn1-DIO-mCherry virus into the audTRN and
915 implanted with an optic fiber. We recorded from MGB neurons in awake head-fixed mice. We presented a
916 set of pure tones in light-on and light-off conditions. **B**. We presented light in the audTRN of PV mice while
917 recording from neurons in the MGB using a vertical multi-channel electrode that spanned the depth of
918 dMGB and vMGB. **C.** Mean PSTH of recorded neurons in MGB. Light-only trials (green line), tone-only
919 trials (black line), and tone- and laser-on trials (light blue line). **D**. Scatter plot of the mean FR for laser off
920 and laser on conditions 0-25 ms (left), 25-50 ms (center), 50-75 ms (right) post-stimulus onset. *Shaded*
921 *areas represent SEM±. N=85, n = 2; n.s. for all periods.*
922
923 **Supplementary Figure S10. Control experiments for optogenetic manipulation of SST^{TRN}**
924 **neurons. A.** SST mice were injected with an AAV5-hSyn1-DIO-mCherry virus into the audTRN and
925 implanted with an optic fiber. We recorded from MGB neurons in awake head-fixed mice. We presented a
926 set of pure tones in light-on and light-off conditions. **B**. We presented light in the audTRN of SST mice while
927 recording from neurons in the MGB using a vertical multi-channel electrode that spanned the depth of
928 dMGB and vMGB. **C.** Mean PSTH of recorded neurons in MGB. Light-only trials (green line), tone-only
929 trials (black line), and tone- and laser-on trials (light blue line). **D**. Scatter plot of the mean FR for laser off
930 and laser on conditions 0-25 ms (left), 25-50 ms (center), 50-75 ms (right) post-stimulus onset. *Shaded*
931 *areas represent SEM±. N=137, n = 2; p-value = n.s. (0-25 ms); 0.006 (25-50 ms), p = 0.000002 (50-75*
932 *ms).*
933

934 ## REFERENCES

935 1. Blackwell, J.M., and Geffen, M.N. (2017). Progress and challenges for understanding the function of
936 cortical microcircuits in auditory processing. Nat. Commun. *8*, 2165. https://doi.org/10.1038/s41467-
937 017-01755-2.

938 2. Chen, Q.C., and Jen, P.H. (2000). Bicuculline application affects discharge patterns, rate-intensity
939 functions, and frequency tuning characteristics of bat auditory cortical neurons. Hear. Res. *150*, 161–
940 174. https://doi.org/10.1016/s0378-5955(00)00197-0.

941 3. Wu, G.K., Arbuckle, R., Liu, B.H., Tao, H.W., and Zhang, L.I. (2008). Lateral sharpening of cortical
942 frequency tuning by approximately balanced inhibition. Neuron *58*, 132–143.
943 https://doi.org/10.1016/j.neuron.2008.01.035.

944 4. Wang, J., Caspary, D., and Salvi, R.J. (2000). GABA-A antagonist causes dramatic expansion of tuning in
945 primary auditory cortex. Neuroreport *11*, 1137–1140.

946 5. Pollak, G.D., Xie, R., Gittelman, J.X., Andoni, S., and Li, N. (2011). The dominance of inhibition in the
947 inferior colliculus. Hear. Res. *274*, 27–39. https://doi.org/10.1016/j.heares.2010.05.010.

948 6. Myoga, M.H., Lehnert, S., Leibold, C., Felmy, F., and Grothe, B. (2014). Glycinergic inhibition tunes
949 coincidence detection in the auditory brainstem. Nat. Commun. *5*, 3790.
950 https://doi.org/10.1038/ncomms4790.

951 7. Burger, R.M., Fukui, I., Ohmori, H., and Rubel, E.W. (2011). Inhibition in the balance: binaurally
952 coupled inhibitory feedback in sound localization circuitry. J. Neurophysiol. *106*, 4–14.
953 https://doi.org/10.1152/jn.00205.2011.

954 8. Natan, R.G., Briguglio, J.J., Mwilambwe-Tshilobo, L., Jones, S.I., Aizenberg, M., Goldberg, E.M., and
955 Geffen, M.N. (2015). Complementary control of sensory adaptation by two types of cortical
956 interneurons. eLife *4*. https://doi.org/10.7554/eLife.09868.

957 9. Natan, R.G., Rao, W., and Geffen, M.N. (2017). Cortical Interneurons Differentially Shape Frequency
958 Tuning following Adaptation. Cell Rep. *21*, 878–890. https://doi.org/10.1016/j.celrep.2017.10.012.

959 10. Aizenberg, M., Mwilambwe-Tshilobo, L., Briguglio, J.J., Natan, R.G., and Geffen, M.N. (2015).
960 Bidirectional Regulation of Innate and Learned Behaviors That Rely on Frequency Discrimination by
961 Cortical Inhibitory Neurons. PLoS Biol. *13*, 1–32. https://doi.org/10.1371/journal.pbio.1002308.

962 11. Briguglio, J.J., Aizenberg, M., Balasubramanian, V., and Geffen, M.N. (2018). Cortical neural activity
963 predicts sensory acuity under optogenetic manipulation. J. Neurosci. *38*, 2094–2105.
964 https://doi.org/10.1523/JNEUROSCI.2457-17.2017.

965 12. Park, Y., and Geffen, M.N. (2019). A Unifying Mechanistic Model of the Auditory Cortex with Inhibitory
966 Subtypes. bioRxiv, 626358. https://doi.org/10.1101/626358.

967 13. Phillips, E.A., and Hasenstaub, A.R. (2016). Asymmetric effects of activating and inactivating cortical
968 interneurons. eLife *5*. https://doi.org/10.7554/eLife.18383.

969 14. Phillips, E.A.K., Schreiner, C.E., and Hasenstaub, A.R. (2017). Cortical Interneurons Differentially
970 Regulate the Effects of Acoustic Context. Cell Rep. *20*, 771–778.
971 https://doi.org/10.1016/j.celrep.2017.07.001.

972 15. Moore, A.K., and Wehr, M. (2013). Parvalbumin-expressing inhibitory interneurons in auditory cortex
973 are well-tuned for frequency. J. Neurosci. *33*, 13713–13723.
974 https://doi.org/10.1523/JNEUROSCI.0663-13.2013.

975 16. Li, L.Y., Xiong, X.R., Ibrahim, L.A., Yuan, W., Tao, H.W., and Zhang, L.I. (2015). Differential Receptive
976 Field Properties of Parvalbumin and Somatostatin Inhibitory Neurons in Mouse Auditory Cortex.
977 Cereb. Cortex *25*, 1782–1791. https://doi.org/10.1093/cercor/bht417.

978 17. Hamilton, L.S., Sohl-Dickstein, J., Huth, A.G., Carels, V.M., Deisseroth, K., and Bao, S. (2013).
979 Optogenetic Activation of an Inhibitory Network Enhances Feedforward Functional Connectivity in
980 Auditory Cortex. Neuron *80*, 1066–1076. https://doi.org/10.1016/j.neuron.2013.08.017.

981 18. Seybold, B.A., Phillips, E.A.K., Schreiner, C.E., and Hasenstaub, A.R. (2015). Inhibitory Actions Unified
982 by Network Integration. Neuron *87*, 1181–1192. https://doi.org/10.1016/J.NEURON.2015.09.013.

983 19. Ulanovsky, N., Las, L., and Nelken, I. (2003). Processing of low-probability sounds by cortical neurons.
984 Nat. Neurosci. *6*, 391–398. https://doi.org/10.1038/nn1032.

985 20. Taaseh, N., Yaron, A., and Nelken, I. (2011). Stimulus-Specific Adaptation and Deviance Detection in
986 the Rat Auditory Cortex. PLoS ONE *6*, e23369. https://doi.org/10.1371/journal.pone.0023369.

987 21. Fishman, Y.I., and Steinschneider, M. (2012). Searching for the mismatch negativity in primary
988 auditory cortex of the awake monkey: Deviance detection or stimulus specific adaptation? J. Neurosci.
989 *32*, 15747–15758. https://doi.org/10.1523/JNEUROSCI.2835-12.2012.

990 22. Farley, B.J., Quirk, M.C., Doherty, J.J., and Christian, E.P. (2010). Stimulus-Specific Adaptation in
991 Auditory Cortex Is an NMDA-Independent Process Distinct from the Sensory Novelty Encoded by the
992 Mismatch Negativity. J. Neurosci. *30*, 16475–16484. https://doi.org/10.1523/JNEUROSCI.2793-
993 10.2010.

994 23. Polterovich, A., Jankowski, M.M., and Nelken, I. (2018). Deviance sensitivity in the auditory cortex of
995 freely moving rats. PLoS ONE *13*, e0197678. https://doi.org/10.1371/journal.pone.0197678.

996 24. Bartlett, E.L. (2013). The organization and physiology of the auditory thalamus and its role in
997 processing acoustic features important for speech perception. Brain Lang. *126*, 29–48.
998 https://doi.org/10.1016/j.bandl.2013.03.003.

999 25. He, J. (2003). Corticofugal modulation of the auditory thalamus. Exp. Brain Res. *153*, 579–590.
1000 https://doi.org/10.1007/s00221-003-1680-5.

1001 26. Crabtree, J.W. (1998). Organization in the auditory sector of the cat's thalamic reticular nucleus. J.
1002 Comp. Neurol. *390*, 167–182. https://doi.org/10.1002/(sici)1096-9861(19980112)390:2<167::aid-
1003 cne1>3.0.co;2-%23.

1004 27. Crabtree, J.W. (2018). Functional diversity of thalamic reticular subnetworks. Front. Syst. Neurosci. *12*,
1005 41. https://doi.org/10.3389/FNSYS.2018.00041/BIBTEX.

1006 28. Houser, C.R., Vaughn, J.E., Barber, R.P., and Roberts, E. (1980). GABA neurons are the major cell type
1007 of the nucleus reticularis thalami. Brain Res. *200*, 341–354. https://doi.org/10.1016/0006-
1008 8993(80)90925-7.

1009 29. Pinault, D. (2004). The thalamic reticular nucleus: structure, function and concept. Brain Res. Rev. *46*,
1010 1–31. https://doi.org/10.1016/J.BRAINRESREV.2004.04.008.

1011 30. Guillery, R.W., and Sherman, S.M. (2002). Thalamic relay functions and their role in corticocortical
1012 communication: generalizations from the visual system. Neuron *33*, 163–175.

1013 31. Carroll, B.J., Sampathkumar, V., Kasthuri, N., and Sherman, S.M. (2022). Layer 5 of cortex innervates
1014 the thalamic reticular nucleus in mice. Proc. Natl. Acad. Sci. U. S. A. *119*.
1015 https://doi.org/10.1073/PNAS.2205209119.

1016 32. Gentet, L.J., and Ulrich, D. (2004). Electrophysiological characterization of synaptic connections
1017 between layer VI cortical cells and neurons of the nucleus reticularis thalami in juvenile rats. Eur. J.
1018 Neurosci. *19*, 625–633. https://doi.org/10.1111/j.1460-9568.2004.03168.x.

1019 33. Guo, W., Clause, A.R., Barth-Maron, A., and Polley, D.B. (2017). A Corticothalamic Circuit for Dynamic
1020 Switching between Feature Detection and Discrimination. Neuron *95*, 180-194.e5.
1021 https://doi.org/10.1016/j.neuron.2017.05.019.

1022 34. Lam, Y.W., and Sherman, S.M. (2005). Mapping by laser photostimulation of connections between the
1023 thalamic reticular and ventral posterior lateral nuclei in the rat. J. Neurophysiol. *94*, 2472–2483.
1024 https://doi.org/10.1152/jn.00206.2005.

1025 35. Lam, Y.W., and Sherman, S.M. (2011). Functional organization of the thalamic input to the thalamic
1026 reticular nucleus. J. Neurosci. *31*, 6791–6799. https://doi.org/10.1523/JNEUROSCI.3073-10.2011.

1027 36. Ahrens, S., Jaramillo, S., Yu, K., Ghosh, S., Hwang, G.R., Paik, R., Lai, C., He, M., Huang, Z.J., and Li, B.
1028 (2015). ErbB4 regulation of a thalamic reticular nucleus circuit for sensory selection. Nat. Neurosci. *18*,
1029 104–111. https://doi.org/10.1038/nn.3897.

1030 37. Crick, F. (2006). Function of the thalamic reticular complex: the searchlight hypothesis. Proc. Natl.
1031 Acad. Sci. *81*, 4586–4590. https://doi.org/10.1073/pnas.81.14.4586.

1032 38. Halassa, M.M., Chen, Z., Wimmer, R.D., Brunetti, P.M., Zhao, S., Zikopoulos, B., Wang, F., Brown, E.N.,
1033 and Wilson, M.A. (2014). State-dependent architecture of thalamic reticular subnetworks. Cell *158*,
1034 808–821. https://doi.org/10.1016/j.cell.2014.06.025.

1035 39. Nakajima, M., Schmitt, L.I., and Halassa, M.M. (2019). Prefrontal Cortex Regulates Sensory Filtering
1036 through a Basal Ganglia-to-Thalamus Pathway. Neuron *103*, 445-458.e10.
1037 https://doi.org/10.1016/j.neuron.2019.05.026.

1038 40. Schmitt, L.I., Wimmer, R.D., Nakajima, M., Happ, M., Mofakham, S., and Halassa, M.M. (2017).
1039 Thalamic amplification of cortical connectivity sustains attentional control. Nature *545*, 219–223.
1040 https://doi.org/10.1038/nature22073.

1041 41. Wimmer, R.D., Schmitt, L.I., Davidson, T.J., Nakajima, M., Deisseroth, K., and Halassa, M.M. (2015).
1042 Thalamic control of sensory selection in divided attention. Nature *526*, 705–709.
1043 https://doi.org/10.1038/nature15398.

1044 42. Martinez-Garcia, R.I., Voelcker, B., Zaltsman, J.B., Patrick, S.L., Stevens, T.R., Connors, B.W.,
1045 Cruikshank, S.J., and Carney, N.D. (2020). Two dynamically distinct circuits drive inhibition in the
1046 sensory thalamus. Nature *583*. https://doi.org/10.1038/s41586-020-2512-5.

1047 43. Clemente-Perez, A., Makinson, S.R., Higashikubo, B., Brovarney, S., Cho, F.S., Urry, A., Holden, S.S.,
1048 Wimer, M., Dávid, C., Fenno, L.E., et al. (2017). Distinct Thalamic Reticular Cell Types Differentially
1049 Modulate Normal and Pathological Cortical Rhythms. Cell Rep. *19*, 2130–2142.
1050 https://doi.org/10.1016/j.celrep.2017.05.044.

1051 44. Li, Y., Lopez-Huerta, V.G., Adiconis, X., Levandowski, K., Choi, S., Simmons, S.K., Arias-Garcia, M.A.,
1052 Guo, B., Yao, A.Y., Blosser, T.R., et al. (2020). Distinct subnetworks of the thalamic reticular nucleus.
1053 Nature *583*. https://doi.org/10.1038/s41586-020-2504-5.

1054 45. Vaughn, M.J., Laswick, Z., Wang, H., and Haas, J.S. (2024). Functionally Distinct Circuits Are Linked by
1055 Heterocellular Electrical Synapses in the Thalamic Reticular Nucleus. eNeuro *11*.
1056 https://doi.org/10.1523/ENEURO.0269-23.2023.

1057 46. Lu, E., Llano, D.A., and Sherman, S.M. (2009). Different distributions of calbindin and calretinin
1058 immunostaining across the medial and dorsal divisions of the mouse medial geniculate body. Hear.
1059 Res. *257*, 16–23. https://doi.org/10.1016/J.HEARES.2009.07.009.

1060 47. Mahn, M., Gibor, L., Patil, P., Cohen-Kashi Malina, K., Oring, S., Printz, Y., Levy, R., Lampl, I., and Yizhar,
1061 O. (2018). High-efficiency optogenetic silencing with soma-targeted anion-conducting
1062 channelrhodopsins. Nat. Commun. *9*, 4125. https://doi.org/10.1038/s41467-018-06511-8.

1063 48. Pham, T., and Haas, J.S. (2018). Electrical synapses between inhibitory neurons shape the responses of
1064 principal neurons to transient inputs in the thalamus: a modeling study. Sci. Rep. *8*, 7763.
1065 https://doi.org/10.1038/s41598-018-25956-x.

1066 49. Pham, T., and Haas, J.S. (2019). Electrical synapses regulate both subthreshold integration and
1067 population activity of principal cells in response to transient inputs within canonical feedforward
1068 circuits. PLOS Comput. Biol. *15*, e1006440. https://doi.org/10.1371/journal.pcbi.1006440.

1069 50. Hou, G., Smith, A.G., and Zhang, Z.-W. (2016). Lack of intrinsic GABAergic connections in the thalamic
1070 reticular nucleus of the mouse. J. Neurosci. *36*, 7246–7252.

1071 51. Deleuze, C., and Huguenard, J.R. (2006). Distinct Electrical and Chemical Connectivity Maps in the
1072 Thalamic Reticular Nucleus: Potential Roles in Synchronization and Sensation. J. Neurosci. *26*, 8633–
1073 8645. https://doi.org/10.1523/JNEUROSCI.2333-06.2006.

1074 52. Lam, Y.-W., Nelson, C.S., and Sherman, S.M. (2006). Mapping of the Functional Interconnections
1075 Between Thalamic Reticular Neurons Using Photostimulation. J. Neurophysiol. *96*, 2593–2600.
1076 https://doi.org/10.1152/jn.00555.2006.

1077 53. Pinault, D., and Deschênes, M. (1998). Projection and innervation patterns of individual thalamic
1078 reticular axons in the thalamus of the adult rat: A three-dimensional, graphic, and morphometric
1079 analysis. J. Comp. Neurol. *391*, 180–203. https://doi.org/10.1002/(SICI)1096-
1080 9861(19980209)391:2<180::AID-CNE3>3.0.CO;2-Z.

1081 54. Shosaku, A., Kayama, Y., Sumitomo, I., Sugitani, M., and Iwama, K. (1989). Analysis of recurrent
1082 inhibitory circuit in rat thalamus: Neurophysiology of the thalamic reticular nucleus. Prog. Neurobiol.
1083 *32*, 77–102. https://doi.org/10.1016/0301-0082(89)90011-7.

1084 55. Crabtree, J.W., Collingridge, G.L., and Isaac, J.T.R. (1998). A new intrathalamic pathway linking
1085 modality-related nuclei in the dorsal thalamus. Nat. Neurosci. *1*, 389–394.
1086 https://doi.org/10.1038/1603.

1087 56. Crabtree, J.W., and Isaac, J.T.R. (2002). New Intrathalamic Pathways Allowing Modality-Related and
1088 Cross-Modality Switching in the Dorsal Thalamus. J. Neurosci. *22*, 8754–8761.
1089 https://doi.org/10.1523/JNEUROSCI.22-19-08754.2002.

1090 57. Kimura, A. (2014). Diverse subthreshold cross-modal sensory interactions in the thalamic reticular
1091 nucleus: implications for new pathways of cross-modal attentional gating function. Eur J Neurosci *39*,
1092 1405–1418.

1093 58. Kimura, A. (2024). Cross-modal sensitivities to auditory and visual stimulations in the first-order
1094 somatosensory thalamic nucleus. Eur. J. Neurosci. *60*, 5621–5657. https://doi.org/10.1111/ejn.16510.

1095 59. Landisman, C.E., and Coulon, P. (2024). A Mixed Electrical and Chemical Synapse in the Thalamic
1096 Reticular Nucleus. J. Neurophysiol. https://doi.org/10.1152/jn.00339.2024.

1097 60. Deschesˆnes, M., Madariaga-Domich, A., and Steriade, M. (1985). Dendrodendritic synapses in the cat
1098 reticularis thalami nucleus: a structural basis for thalamic spindle synchronization. Brain Res. *334*,
1099 165–168. https://doi.org/10.1016/0006-8993(85)90580-3.

1100 61. Yen, C.T., Conley, M., Hendry, S.H., and Jones, E.G. (1985). The morphology of physiologically
1101 identified GABAergic neurons in the somatic sensory part of the thalamic reticular nucleus in the cat.
1102 J. Neurosci. Off. J. Soc. Neurosci. *5*, 2254–2268. https://doi.org/10.1523/JNEUROSCI.05-08-
1103 02254.1985.

1104 62. Asanuma, C., and Porter, L.L. (1990). Light and electron microscopic evidence for a GABAergic
1105 projection from the caudal basal forebrain to the thalamic reticular nucleus in rats. J. Comp. Neurol.
1106 *302*, 159–172. https://doi.org/10.1002/cne.903020112.

1107 63. Herrera, C.G., Cadavieco, M.C., Jego, S., Ponomarenko, A., Korotkova, T., and Adamantidis, A. (2015).
1108 Hypothalamic feedforward inhibition of thalamocortical network controls arousal and consciousness.
1109 Nat. Neurosci. *19*, 290–298. https://doi.org/10.1038/nn.4209.

1110 64. Paré, D., Hazrati, L.N., Parent, A., and Steriade, M. (1990). Substantia nigra pars reticulata projects to
1111 the reticular thalamic nucleus of the cat: a morphological and electrophysiological study. Brain Res.
1112 *535*, 139–146. https://doi.org/10.1016/0006-8993(90)91832-2.

1113 65. Asanuma, C. (1989). Axonal arborizations of a magnocellular basal nucleus input and their relation to
1114 the neurons in the thalamic reticular nucleus of rats. Proc. Natl. Acad. Sci. *86*, 4746–4750.
1115 https://doi.org/10.1073/pnas.86.12.4746.

1116 66. Jourdain, A., Semba, K., and Fibiger, H.C. (1989). Basal forebrain and mesopontine tegmental
1117 projections to the reticular thalamic nucleus: an axonal collateralization and immunohistochemical
1118 study in the rat. Brain Res *505*, 55–65. https://doi.org/10.1016/0006-8993(89)90115-7.

1119 67. Bickford, M.E., Gunluk, A.E., Van Horn, S.C., and Sherman, S.M. (1994). GABAergic projection from the
1120 basal forebrain to the visual sector of the thalamic reticular nucleus in the cat. J Comp Neurol *348*,
1121 481–510. https://doi.org/10.1002/cne.903480402.

1122 68. Gandia, J.A., De Las Heras, S., Garcia, M., and Gimenez-Amaya, J.M. (1993). Afferent projections to the
1123 reticular thalamic nucleus from the globus pallidus and the substantia nigra in the rat. Brain Res Bull
1124 *32*, 351–358. https://doi.org/10.1016/0361-9230(93)90199-l.

1125 69. Halassa, M.M., and Acsady, L. (2016). Thalamic Inhibition: Diverse Sources, Diverse Scales. Trends
1126 Neurosci *39*, 680–693. https://doi.org/10.1016/j.tins.2016.08.001.

1127 70. Cornwall, J., Cooper, J.D., and Phillipson, O.T. (1990). Projections to the rostral reticular thalamic
1128 nucleus in the rat. Exp Brain Res *80*, 157–171. https://doi.org/10.1007/bf00228857.

1129 71. Belén Pardi, M., Vogenstahl, J., Dalmay, T., Spanò, T., Pu, D.L., Naumann, L.B., Kretschmer, F.,
1130 Sprekeler, H., and Letzkus, J.J. (2020). A thalamocortical top-down circuit for associative memory.
1131 Science *370*, 844–848.
1132 https://doi.org/10.1126/SCIENCE.ABC2399/SUPPL_FILE/ABC2399_PARDI_SM.PDF.

1133 72. Lee, C.C., and Sherman, S.M. (2010). Drivers and Modulators in the Central Auditory Pathways. Front.
1134 Neurosci. *4*, 79. https://doi.org/10.3389/neuro.01.014.2010.

1135 73. Winer, J.A. (2005). Decoding the auditory corticofugal systems. Hear. Res. *207*, 1–9.
1136 https://doi.org/10.1016/j.heares.2005.06.007.

1137 74. Moore, D.R. (1991). Anatomy and Physiology of Binaural Hearing. Int. J. Audiol. *30*, 125–134.
1138 https://doi.org/10.3109/00206099109072878.

1139 75. Grothe, B., Pecka, M., and McAlpine, D. (2010). Mechanisms of Sound Localization in Mammals.
1140 Physiol. Rev. *90*, 983–1012. https://doi.org/10.1152/physrev.00026.2009.

1141 76. Mellott, J.G., Beebe, N.L., and Schofield, B.R. (2019). Bilateral projections to the thalamus from
1142 individual neurons in the inferior colliculus. J. Comp. Neurol. *527*, 1118–1126.
1143 https://doi.org/10.1002/cne.24600.

1144 77. Johnson, K.R., Tian, C., Gagnon, L.H., Jiang, H., Ding, D., and Salvi, R. (2017). Effects of Cdh23 single
1145 nucleotide substitutions on age-related hearing loss in C57BL/6 and 129S1/Sv mice and comparisons
1146 with congenic strains. Sci. Rep. *7*, 44450. https://doi.org/10.1038/srep44450.

1147 78. Siegle, J.H., López, A.C., Patel, Y.A., Abramov, K., Ohayon, S., and Voigts, J. (2017). Open Ephys: an
1148 open-source, plugin-based platform for multichannel electrophysiology. J. Neural Eng. *14*, 045003.
1149 https://doi.org/10.1088/1741-2552/aa5eea.

1150 79. Pachitariu, M., Sridhar, S., and Stringer, C. (2023). Solving the spike sorting problem with Kilosort.
1151 Preprint at bioRxiv, https://doi.org/10.1101/2023.01.07.523036
1152 https://doi.org/10.1101/2023.01.07.523036.

1153 80. Romero, S., Hight, A.E., Clayton, K.K., Resnik, J., Williamson, R.S., Hancock, K.E., and Polley, D.B.
1154 (2020). Cellular and Widefield Imaging of Sound Frequency Organization in Primary and Higher Order
1155 Fields of the Mouse Auditory Cortex. Cereb. Cortex *30*, 1603–1622.
1156 https://doi.org/10.1093/CERCOR/BHZ190.

1157 81. Horie, M., Tsukano, H., Hishida, R., Takebayashi, H., and Shibuki, K. (2013). Dual compartments of the
1158 ventral division of the medial geniculate body projecting to the core region of the auditory cortex in
1159 C57BL/6 mice. Neurosci. Res. *76*, 207–212. https://doi.org/10.1016/j.neures.2013.05.004.

1160 82. Stringer, C., Wang, T., Michaelos, M., and Pachitariu, M. (2021). Cellpose: a generalist algorithm for
1161 cellular segmentation. Nat. Methods *18*, 100–106. https://doi.org/10.1038/s41592-020-01018-x.

1162 83. Destexhe, A., Bal, T., McCormick, D.A., and Sejnowski, T.J. (1996). Ionic mechanisms underlying
1163 synchronized oscillations and propagating waves in a model of ferret thalamic slices. J. Neurophysiol.
1164 *76*, 2049–2070. https://doi.org/10.1152/jn.1996.76.3.2049.

1165 84. Traub, R.D., Contreras, D., Cunningham, M.O., Murray, H., LeBeau, F.E.N., Roopun, A., Bibbig, A.,
1166 Wilent, W.B., Higley, M.J., and Whittington, M.A. (2005). Single-Column Thalamocortical Network
1167 Model Exhibiting Gamma Oscillations, Sleep Spindles, and Epileptogenic Bursts. J. Neurophysiol. *93*,
1168 2194–2232. https://doi.org/10.1152/jn.00983.2004.

1169 85. Desai, N.V., and Varela, C. (2021). Distinct burst properties contribute to the functional diversity of
1170 thalamic nuclei. J. Comp. Neurol. *529*, 3726–3750. https://doi.org/10.1002/cne.25141.

1171

1172

Table 1. Statistics Table.

Figure	Comparison	N	Mean	Median	SEM	Test	p
1B.	Gray Values; PV-audTRN projections; dMGB vs. vMGB	14	d: 30.18	d: 26.33	d: 2.65	Wilcoxon signed-rank test	0.000
			v: 41.41	v: 39.53	v: 2.65		
1D.	Gray Values; SST-audTRN projections; dMGB vs. vMGB	8	d: 95.04	d: 102.71	d: 17.17	Wilcoxon signed-rank test	0.023
			v: 58.06	v: 62.84	v: 5.83		
2	Δ FR (Hz); PV-facilitated. 2.5-2.9 mm (1st bin) vs. -3.1-3.5 mm (2nd bin)	1st bin: 16	1st bin: 12.45	1st bin: 5.61	1st bin: 3.72	Mann-Whitney U Test	0.008
		2nd bin: 30	2nd bin: 41.66	2nd bin: 24.70	2nd bin: 11.16		
2	Δ FR (Hz); PV-Suppressed. 2.5-2.9 mm (1st bin) vs. -3.1-3.5 mm (2nd bin)	1st bin: 30	1st bin: -10.35	1st bin: -9.60	1st bin: 0.97	Mann-Whitney U Test	0.219
		2nd bin: 39	2nd bin: -15.31	2nd bin: -12.28	2nd bin: 2.14		
2	Δ FR (Hz); SST-facilitated. 2.5-2.9 mm (1st bin) vs. -3.1-3.5 mm (2nd bin)	1st bin: 0	1st bin: n/a	1st bin: n/a	1st bin: n/a	n/a	n/a
		2nd bin: 2	2nd bin: 6.57	2nd bin: 6.57	2nd bin: 0.48		
2	Δ FR (Hz); SST-Suppressed; 2.5-2.9 mm (1st bin) vs. -3.1-3.5 mm (2nd bin)	1st bin: 51	1st bin: -13.46	1st bin: -10.85	1st bin: 1.29	Mann-Whitney U Test	0.012
		2nd bin: 66	2nd bin: -10.37	2nd bin: -7.08	2nd bin: 1.3		
3	Light responses (Hz), PV-facilitated, light Only vs. light diff (tone+light – tone only) vs, 0-25 ms,	74	Light Only: 29.19	Light Only: 11.45	Light Only: 6.35	Wilcoxon signed-rank test t	0.0113
			Light diff: 33.47	Light diff: 13.37	Light diff: 6.35		
3	Light responses (Hz), PV-suppressed, light Only vs. light diff (tone+light – tone only) vs, 0-25 ms	104	Light-Only: - 2.75	Light-Only: - 2.53	Light-Only: 0.66	Wilcoxon signed-rank test t	1.16e-12
			Light diff: -12.59	Light diff: -10.10	Light diff: 1.02		
3	Time to peak (ms); PV-Facilitated: $Light_{Off}$ vs. $Light_{On}$	74	Off: 12.27	Off: 12.0	Off: 0.70	Wilcoxon signed-rank test	0.0398
			On: 13.7	On: 14.0	On: 0.56		
3		104	Off: 9.19	Off: 8	Off: 0.51		0.070

	Time to peak (ms); PV-Suppressed: $Light_{Off}$ vs. $Light_{On}$		On: 8.73	On: 8	On: 0.53	Wilcoxon signed-rank test	
3	Firing Rate (Hz) 0-25 ms; PV Facilitated: $Light_{Off}$ vs. $Light_{On}$	74	Off: 14.58	Off: 7.20	Off: 2.118	Wilcoxon signed-rank test	0.00000
			On: 48.05	On: 28.78	On: 6.85		
3	Firing Rate (Hz) 0-25 ms; PV-Suppressed: $Light_{Off}$ vs. $Light_{On}$	104	Off: 24.34	Off: 17.71	Off: 1.93	Wilcoxon signed-rank test	0.00000
			On: 11.76	On: 5.02	On: 1.37		
3	Firing Rate (Hz) 25-50 ms; PV Facilitated: $Light_{Off}$ vs. $Light_{On}$	74	Off: 22.45	Off: 14.57	Off: 2.96	Wilcoxon signed-rank test	0.00004
			On: 36.40	On: 24.72	On: 4.97		
3	Firing Rate (Hz) 25-50 ms; PV Suppressed: $Light_{Off}$ vs. $Light_{On}$	104	Off: 14.96	Off: 7.42	Off: 2.67	Wilcoxon signed-rank test	0.00000
			On: 4.88	On: 1.27	On: 1.13		
3	Light responses (Hz), PV-facilitated, light Only vs. light diff (tone+light – tone only) vs, 0-25 ms,	74	Light Only: 29.19	Light Only: 11.45	Light Only: 6.35	Wilcoxon signed-rank test t	0.0113
			Light diff: 33.47	Light diff: 13.37	Light diff: 6.35		
3	Light responses (Hz), PV-suppressed, light Only vs. light diff (tone+light – tone only) vs, 0-25 ms	104	Light-Only: - 2.75	Light-Only: - 2.53	Light-Only: 0.66	Wilcoxon signed-rank test t	1.16e-12
			Light diff: -12.59	Light diff: -10.10	Light diff: 1.02		
4	Time to peak (ms); SST Facilitated: $Light_{Off}$ vs. $Light_{On}$	4	Off: 12.0	Off: 11	Off: 2.16	Wilcoxon signed-rank test	1
			On: 12.0	On: 12	On: 2.58		
4	Time to peak (ms); SST Suppressed: $Light_{Off}$ vs. $Light_{On}$	181	Off: 9.23	Off: 8	Off: 0.378	Wilcoxon signed-rank test	0.071
			On: 8.95	On: 6	On: 0.421		
4	Firing Rate (Hz), 0-25 ms; SST Facilitated: $Light_{Off}$ vs. $Light_{On}$	4	Off: 30.31	Off: 32.41	Off: 8.42	Wilcoxon signed-rank test	0.125
			On: 36.34	On: 38.74	On: 8.30		
4	Firing Rate (Hz), 0-25 ms; SST Suppressed: $Light_{Off}$ vs. $Light_{On}$	181	Off: 24.43	Off: 16.19	Off: 1.73	Wilcoxon signed-rank test	0.00000000
			On: 12.86	On: 6.19	On: 1.24		
4	Firing Rate (Hz) 25-50 ms; SST Facilitated: $Light_{Off}$ vs. $Light_{On}$	4	Off: 8.51	Off: 5.07	Off: 4.63	Wilcoxon signed-rank test	0.125
			On: 12.86	On: 6.19	On: 1.24		
4	Firing Rate (Hz) 25-50 ms; SST Suppressed: $Light_{Off}$ vs. $Light_{On}$	181	Off: 10.59	Off: 5.22	Off: 1.22	Wilcoxon signed-rank test	0.00000
			On: 7.39	On: 2.23	On: 1.05		

4	Light responses (Hz), SST-Facilitated, light Only vs. light diff (tone+light – tone only) vs, 0-25 ms,	4	Light Only: -4.23	Light Only: -2.49	Light Only: 2.74	Wilcoxon signed-rank test	0.026
			Light diff: 6.038	Light diff: 5.86	Light diff: 0.37		
4	Light responses (Hz), SST-Suppressed, light Only vs. light diff (tone+light – tone only) vs, 0-25 ms,	181	Light Only: -4.21	Light Only: -2.17	Light Only: 0.47	Wilcoxon signed-rank test	3.8e-18
			Light diff: -11.57	Light diff: -7.91	Light diff: 0.80		
5	Sparseness, 0-25 ms; PV Facilitated. $Light_{Off}$ vs. $Light_{On}$	74	Off: 0.476	Off: 0.487	Off: 0.030	Wilcoxon signed-rank test	0.000
			On: 0.179	On: 0.122	On: 0.020		
5	Sparseness, 0-25 ms; PV Suppressed. $Light_{Off}$ vs. $Light_{On}$	104	Off: 0.383	Off: 0.356	Off: 0.017	Wilcoxon signed-rank test	0.00000009
			On: 0.468	On: 0.454	On: 0.020		
5	Sparseness, 0-25 ms; SST Facilitated. $Light_{Off}$ vs. $Light_{On}$	4	Off: 0.249	Off: 0.273	Off: 0.044	Wilcoxon signed-rank test	0.125
			On: 0.167	On: 0.159	On: 0.028		
5	Sparseness, 0-25 ms; SST Suppressed. $Light_{Off}$ vs. $Light_{On}$	181	Off: 0.361	Off: 0.332	Off: 0.013	Wilcoxon signed-rank test	0.00000000
			On: 0.518	On: 0.518	On: 0.015		
S6	Mu (change, Hz), PV Suppressed. $Light_{Off}$ vs. $Light_{On}$	26	-3159.1	209.2		Wilcoxon signed-rank test	1
S6	Mu (change, Hz). PV Facilitated. $Light_{Off}$ vs. $Light_{On}$	11	-1308.2	-497.1		Wilcoxon signed-rank test	0.465
S6	Sigma (change). PV Facilitated. $Light_{Off}$ vs. $Light_{On}$	11	0.068	.0.03		Wilcoxon signed-rank test	0.278
S6	Sigma (change). PV Suppressed. $Light_{Off}$ vs. $Light_{On}$	26	-0.124	-0.072		Wilcoxon signed-rank test	0.027
S6	Mu (change, Hz). SST Facilitated. $Light_{Off}$ vs. $Light_{On}$	0	n/a	n/a	n/a		
S6	Mu (change, Hz). SST Suppressed. $Light_{Off}$ vs. $Light_{On}$	47	2672.5	156.1		Wilcoxon signed-rank test	0.021

S6	Sigma (change). SST Facilitated. $Light_{Off}$ vs. $Light_{On}$	0	n/a	n/a	n/a		
S6	Sigma (change). SST Suppressed. $Light_{Off}$ vs. $Light_{On}$	47	-0.19	-0.06		Wilcoxon signed-rank test	0.0002
S9	Firing Rate (Hz), 0-25 ms; PV-Cre, mCherry (no opsin): $Light_{Off}$ vs. $Light_{On}$	85	Off: 14.76 On: 15.08	Off: 8.10 On: 8.70	Off: 2.31 On: 2.30	Wilcoxon signed-rank test	0.087
S9	Firing Rate (Hz) 25-50 ms; PV-Cre, mCherry (no opsin): $Light_{Off}$ vs. $Light_{On}$	85	Off: 6.98 On: 9.50	Off: 3.73 On: 3.92	Off: 1.08 On: 1.72	Wilcoxon signed-rank test	0.762
S9	Firing Rate (Hz) 50-75 ms; PV-Cre, mCherry (no opsin): $Light_{Off}$ vs. $Light_{On}$	85	Off: 5.79 On: 7.05	Off: 4.16 On: 4.02	Off: 0.75 On: 0.91	Wilcoxon signed-rank test	0.434
S10	Firing Rate (Hz), 0-25 ms; SST-Cre, mCherry (no opsin): $Light_{Off}$ vs. $Light_{On}$	137	Off: 16.19 On: 16.38	Off: 12.61 On: 13.38	Off: 1.24 On: 1.25	Wilcoxon signed-rank test	0.373
S10	Firing Rate (Hz) 25-50 ms; SST-Cre, mCherry (no opsin): $Light_{Off}$ vs. $Light_{On}$	137	Off: 12.40 On: 15.07	Off: 8.53 On: 10.53	Off: 1.08 On: 1.36	Wilcoxon signed-rank test	0.006
S10	Firing Rate (Hz) 50-75 ms; SST-Cre, mCherry (no opsin): $Light_{Off}$ vs. $Light_{On}$	137	Off: 9.99 On: 12.25	Off: 7.95 On: 8.92	Off: 0.72 On: 0.95	Wilcoxon signed-rank test	0.000002